Modeling Multi-Scale Deformation Cycles in Subduction Zones with a Continuum Visco-Elastic-Brittle Framework

Véronique Dansereau [1], Nikolai Shapiro[1], Michel Campillo[1], Jérôme Weiss[1]

[1]Institut des Sciences de la Terre, Université Grenoble Alpes, CNRS (5275), Grenoble, France

Key Points:

- We present a continuum model for the deformation of faults in which the mechanical strength vary continuously as a function of the damage.
- The model's numerical scheme allows covering the very short and very long time scale processes involved in the slow earthquake phenomenon.
- The model reproduces different types of transient deformations, akin to slow and classical earthquakes in subduction zones.

Corresponding author: Véronique Dansereau, veronique.dansereau@univ-grenoble-alpes.fr

Abstract

The overwhelming amount of seismic, geodesic and in-situ observations accumulated over the last 30 years clearly indicate that, from a mechanical point of view, faults should be considered as both damageable elastic solids in which highly localized features emerge as a result of very short-term brittle processes and materials experiencing ductile strains distributed in large volumes and over long time scales. The interplay of both deformation mechanisms, brittle and ductile, give rise to transient phenomena associating slow slip and tremors, known as slow earthquakes, which dissipate a significant amount of stress in the fault system. The physically-based numerical models developed to improve our comprehension of the mechanical and dynamical behaviour of faults must therefore have the capacity to treat simultaneously both deformation mechanisms and to cover a wide range of time scales in a numerically efficient manner. This capability is essential, both for simulating accurately their deformation cycles and for improving our interpretation of the available observations.

In this paper, we present a numerically efficient visco-elasto-brittle numerical framework that can simulate transient deformations akin to that observed in the context of subduction zones, over the wide range of time scales relevant for slow earthquakes. We implement the model in idealized simple shear simulations and explore the sensitivity of its behaviour to the value of its main mechanical parameters.

Plain Language Summary

The outer part of the Earth, called the lithosphere, is a complex object that deforms both in a solid and a fluid manner. Where tectonic plates meet, such as in fault zones, this duality gives rise to a variety of phenomena. The solid behaviour is associated with earthquakes and very sudden slip movements of the fault that we feel at the surface. The fluid behaviour translates into a slow and steady slip at depth. In between, the mixed solid-fluid behaviour results in progressive accelerations and decelerations of the fault slip accompanied with very weak quakes, which are called *slow earthquakes*. These slow earthquakes modulate the deformation cycle of faults and most probably impact the occurrence of "real", or *classical*, earthquakes. It is therefore important to account for them in numerical models that aim to help us understand this cycle better. In this paper we present a model of the deformation of fault zones that we have developed with the particular goal of representing slow earthquakes and that allows the lithosphere to behave sometimes like a solid, sometimes like a fluid.

1 Introduction

Earth's materials are known to exhibit a variety of deformation mechanisms depending on temperature, pressure and loading conditions as well as on the time and spatial scales at which they are observed (e.g., Burov, 2011). In the most dynamic parts of the Earth's lithosphere, such as plate boundaries and fault zones, volcanic systems and landslides, the interplay between different mechanisms can result in a strong strain localization and a complex temporal behaviour. The slow deformation occurring over geological time scales can indeed be suddenly accelerated and give rise to catastrophic events (earthquakes, eruptions, landslides) that release huge amounts of energy in a very short time.

Historically, the deformation of the lithosphere has been studied either at the short time scales (seconds to minutes) of these catastrophic events or at the very large time scales (years to millions of years) of plate tectonic motion. However, the technological progresses in observational systems over the last 30 years has brought about a revolution in the comprehension of its dynamical behaviour, by allowing to explore the time scales in between. Global Positioning System (GPS), radar interferometry (Synthetic Aperture Radar, InSAR) and satellite gravimetry data have indeed driven a huge leap forward in terms of measuring the deformation of the Earth surface continuously in time and space and at high resolution. These new geodetic observations have been accompanied by rapid deployments of dense seismic networks and by the emergence of novel methods of analysis of continuous seismic data that allow exploring deformation mechanisms over a significantly wider range of time scales.

In the case of earthquakes, the occurrence of co-seismic rupture processes that redistribute Coulomb stresses over short time scales (on the order of seconds) and the associated scaling properties have been established for a long time (Omori, 1894; Gutemberg & Richter, 1949; Turcotte, 1992). However, the recent advances in the observational systems and data analysis methods have profoundly modified our vision of how plate tectonic motions are accommodated and how stresses are dissipated along faults. In particular, the combination of high resolution geodetic and seismic data has resulted in improved tracking of co-, post- and inter-seismic deformation patterns (e.g., K. Wang et al., 2012) and in the discovery of new types of transient phenomena designated as "slow earthquakes". These slow earthquakes, associated because of their triggering depth with the so-called brittle-ductile transition comprised between the brittle, seismic zone near the surface and the ductile, aseismic zone below (e.g., Dragert et al., 2004; Peng & Gomberg, 2010; Obara & Kato, 2016, and many others), combine periodic accelerations of the fault slip with weak seismic radiations known as tectonic tremors (e.g., Dragert et al., 2001; Obara, 2002; Peng & Gomberg, 2010). Analyses based on the cross-correlations of ambient seismic noise have demonstrated that the transient deformations accompanying both slow and major earthquakes are associated with changes in elastic properties of the material in the vicinity of the fault, reminiscent of damaging processes and of a non-elastic, or at least nonlinear elastic behaviour (e.g., Brenguier et al., 2008; Rivet et al., 2011; Q.-Y. Wang et al., 2019). Seismic data (e.g., Audet et al., 2009), along with other sources such as tomographic imagery (Shelly et al., 2006) and the observation of exhumed subduction zones (Angiboust et al., 2015), have also allowed identifying fluids as another major player in the transient deformation of faults. In the context of slow earthquakes in particular, the increased pore-pressure from fluids trapped in the fault zone and associated pore-pressure variations and diffusion are indeed believed to partially control the seismic and slow slip activity via the weakening and fracturing of the host rock, the local reduction of the effective stress and friction along the shearing plane and the triggering and migration of tremors (e.g., Brown et al., 2005; Frank, Shapiro, et al., 2015; Shapiro et al., 2018; Cruz-Atienza et al., 2018; Dublanchet, 2019; Luo & Liu, 2019, 2021, and many others).

1.1 Existing Modelling Approaches

The direct modelling approaches that exist to model the deformation of the Earth's lithosphere and faults in particular can be divided in several categories.

The first includes continuum frameworks based on a fluid mechanics approach, namely viscous, visco-elastic, visco-plastic or elasto-visco-plastic models. Such models have been developed to represent the diffuse, ductile and potentially large deformations associated with plate tectonics motion, for instance the formation of mountain ranges and continental rifts (e.g., Royden et al., 1997; Frederiksen & Braun, 2001; Popov & Sobolev, 2008). They can reproduce strain localization by including strain-weakening mechanisms, such as a non-linear dependence of the viscous strain rate on the stress and thermo-mechanical feedbacks. However, their applications are restricted to ductile deformations on geological time scales. In the context of faults, visco-elastic models of the Maxwell or Burgers type (see figure 1) have also been often used to represent the mechanical behaviour of the combined Earth's crust and mantle system (e.g. Nur & Mavko, 1974; Pollitz et al., 2001; Pollitz, 2003, 2005; Hetland & Hager, 2005, 2006; K. Wang et al., 2012; Sun & Wang, 2015). In such frameworks, the Maxwell component represents the lithosphere, which can elastically transmit stresses over short time scales, while relaxing stresses in an exponential manner over very long time scales. The Kelvin component is added to represents the more ductile asthenosphere, which hosts mantle convection and is thought to cause a delayed elastic response, measurable in the reversal of surface velocities after a major earthquake (e.g., Sun & Wang, 2015). However, with constant mechanical parameters (elastic moduli and viscosities), these models cannot by themselves account for the rheological stratification of fault zones, nor for the presence of a relatively localized shearing zone that concentrates the deformation. They are therefore usually implemented in "layered" frameworks (e.g., Hetland & Hager, 2005, 2006; K. Wang et al., 2012; Sun & Wang, 2015), in which the structure of the system is prescribed and divided in multiple pre-determined layers with different rheologies (e.g., an elastic layer of crust embedded in a visco-elastic mantle) and is thus not allowed to evolve in time. With constant mechanical parameters also, neither the Maxwell nor the Burgers model can reproduce the transient deformations of fault systems over a wide enough range of time scales (Ingleby & Wright, 2017; Periollat et al., 2022): deformations which translate for instance in an Omori-like decay of post-seismic surface velocity (velocity inversely proportional to the time since the earthquake), observed hours to ten of years after moderate to large continental earthquakes (Ingleby & Wright, 2017).

A second category of models aim to represent the transition between stable and unstable deformation regimes within the Earth crust by assimilating brittle and frictional processes to the problem of friction on a material interface. This is the case for the well-known block-slider framework, a parametric model stemming from experimental studies of the frictional behaviour of various materials including rocks, which combines the principle of linear elasticity and non-linear stick-slip friction between a sliding block and an underlying surface. Purely conceptual models including these basic ingredients have first been used to explain the statistical properties associated with major earthquakes, such as the Gutemberg-Richter law (e.g., Burridge & Knopoff, 1967; Carlson & Langer, 1989). The rheology of frictional interfaces has been later formulated as a constitutive law known as "rate-and-state friction" (Dieterich, 1978, 1979a, 1979b) which has been widely used to model fault instabilities and earthquakes (e.g., Liu & Rice, 2005; Segall & Bradley, 2012, and many others). This law establishes the following relation between the measured friction coefficient, μ, the sliding velocity, V, and the state of the slip plane, θ:

$$\mu(\theta, V) = \mu^* + a \ln \frac{V}{V^*} + b \ln \frac{V^* \theta}{D_c}$$

where μ^* is a friction coefficient at a reference sliding velocity, V^*, a and b are proportionality constants for the magnitude of instantaneous and time-dependant displacements respectively and D_c is a characteristic slip distance for the evolution of the system towards a new stable state. It is often coupled to an evolution equation for the state parameter, θ, which describes aging effects (Dieterich, 1979a; Ruina, 1983). For negative values of $(a-b)$, the model describes a decrease of the friction coefficient with increasing sliding velocity and hence an unstable, velocity-weakening state, assimilated to a brittle, seismic behaviour. For positive values of $(a-b)$, it describes an increase of the friction coefficient with the slip velocity, therefore a state of stable, velocity-hardening slip, assimilated to an aseismic, ductile behaviour. By including additional levels of complexity relevant to faults, which allow a change of sign of $(a-b)$ along the interface (for instance, a dependence of a and b on the temperature), this model can also reproduce transitions between a brittle and a ductile behaviour and transient slip events (Liu & Rice, 2005, 2007; Segall & Bradley, 2012). Its main limitation, however, is that it is empirically-based. As such, its extrapolation to the temporal and spatial scales of geophysical systems such as faults on the basis of the results obtained in the laboratory is not trivial and questionable (e.g., Chen et al., 2017; van den Ende et al., 2018). A second important limitation is that it is an interface rheology, which implies a prescribed, non-evolving location of the sliding plane and which does not take into account its microstructure or its volumetric deformation. By this fact, it presents a limit to which it can be enriched to include the highly relevant physico-chemical, mineralogical and hydro-mechanical processes involved in the fault deformation cycle. It is also important to note that a "fault plane" approach is in contradiction with seismic data and geological observations of exhumed faults, which suggest that the deformation occurs within a core zone made of gouge, sandwiched between a metric to kilometric-scale zone of damaged rocks (Caine et al., 1996; Angiboust et al., 2015; Hayman & Lavier, 2014; Gao & Wang, 2017).

Another category of models include continuum mechanics damage frameworks (e.g., Ashby & Sammis, 1990; Lyakhovsky, Reches, et al., 1997; Tang, 1997; Amitrano et al., 1999; Bhat et al., 2012, and many others). So-called elasto-brittle schemes, which couple a damage variable to an elastic constitutive law, has indeed been used to represent the fracturing processes and the associated strong localization of the deformation in faults (e.g. Lyakhovsky, Ben-Zion, & Agnon, 1997; Lyakhovsky et al., 2001; Ben-Zion & Lyakhovsky, 2002, and later papers). Without accounting for the *dynamic* propagation of fractures nor the generation of seismic waves, these models represent the redistribution of elastic stresses caused by the generation and coalescence of micro-fractures and the complex mechanical interactions in the material that stem from its micro-structural heterogeneity. They thereby present the advantage of simulating the emergence of a damaged shearing or sliding zone (without the need to prescribe its location or geometry), the stable to unstable transition of the system that precedes the macroscopic rupture as well as the scaling laws associated with the localization of the deformation and the spatio-temporal clustering of the seismic activity (e.g., Ben-Zion & Lyakhovsky, 2002; Turcotte et al., 2003; Shcherbakov et al., 2005). An intrinsic limitation of such schemes, however, is that they are based on an elastic constitutive law and as such, they cannot simulate any pre- or post-rupture permanent deformation in the material. By this fact, it cannot reproduce the entire deformation cycle of faults. Hamiel et al., (Hamiel et al., 2004) and Dansereau et al., (Dansereau et al., 2016a) therefore elaborated from elasto-brittle frameworks by adding a viscous relaxation term that is coupled to the local level of damage in order to represent, respectively, the small irreversible deformation that accumulate towards the macro-rupture and the permanent and potentially large post-rupture deformation of the fractured material. Their visco-elasto-brittle models have been shown to successfully simulate the scaling laws associated with brittle deformations in faults (e.g., Ben-Zion & Lyakhovsky, 2006) and a mechanically similar system: sea ice (Dansereau et al., 2016a; Rampal et al., 2019; Ólason et al., 2021). However, in the context of faults, the numerically-coupled treatment of damage propagation and viscous relaxation in these models makes them too computationally expensive to cover the very long time scales associated with ductile deformations and hence reproduce multiple deformation cycles.

Finally, other models have been developed to help understanding the dynamics of fluids and its role in the deformation of faults (e.g. Segall & Rice, 1995, and many others). In particular, recent idealized models of pressure diffusion in the host rock with rapidly varying permeability have been able to explain the observed rapid tremor migrations and their reversals (Cruz-Atienza et al., 2018; Farge et al., 2021). However, a very important challenge remains to day: to couple these models with the two- or three-dimensional deformation of the solid matrix and other near-fault processes to allow assessing their impact on the geodetically observed strains.

1.2 Focus on the Slow Earthquake Phenomenon

Developing a single numerical modeling framework suitable for all of the above mentioned physical processes and that can cover the entire spectrum of associated time scales is a very ambitious, perhaps unachievable, goal. Therefore, in this paper, we focus on modelling the mechanical behaviour and deformation of fault zones, leaving aside for the moment the role of fluids. We also concentrate over time scales intermediate between those characterizing the cycle of major, or "classical", earthquakes (from decades to thousands of years) and the one of dynamic rupture (faster than hundreds of seconds). Within this range, the deformation of faults is often controlled by slow earthquakes.

The slowest temporal scale associated with the slow earthquake phenomenon is revealed by geodetic observations of the accompanied slow and diffuse surface deformation, with typical event durations between weeks and months and inter-events gaps of the order of a few years (e.g., Dragert et al., 2001; Kostoglodov et al., 2003; Radiguet et al., 2012). The fastest temporal scale is related to seismic radiations, observed at frequencies above 1 Hz in the form of tectonic tremors (e.g., Obara, 2002; Payero et al., 2008) or low-frequency earthquakes (LFEs) (e.g., Shelly et al., 2006; Bostock et al., 2012; Frank et al., 2014) and which imply localized, brittle deformations and associated elastic strain variations in the source region on the order of fractions of a second. Therefore, even if ignoring the second-order effect of the long-term deformation of the system attributable to mantle relaxation, convection and delayed elastic deformations, as done in this paper, building a model for slow earthquakes entails dealing with localized, brittle deformations and diffuse, ductile deformations that are separated by about 8 orders of magnitudes of time scales. This huge separation requires developing a numerical scheme that allows simulating the relevant processes in reasonable simulation times.

This is the aim of the current work : developing a physically sound and numerically efficient continuum rheological framework for slow earthquakes. It is important to note however that doing so, we also keep in mind a future application to a wider range of time scales relevant to the entire seismic cycle. Another objective is that this framework be simple and versatile, so that to give valuable insights and eventually be transferable in the context of other geophysical systems that are characterized by a similar dynamics, that is, a dynamics comprised of mixed brittle/ductile and transient deformations, such as landslides and volcanic edifices (e.g., Peng & Gomberg, 2010; Lacroix et al., 2014; Carrier et al., 2015; Got et al., 2017; Handwerger et al., 2016; Poli, 2017; Parisio et al., 2019; Seydoux et al., 2020, and many others). A very important feature of the proposed modelling approach is that it accounts for rock fracturing processes via a progressive damage mechanism that is coupled to the mechanical strength of the material, which is described not only by an elastic modulii but also an apparent viscosity. As such, in addition to the long-term evolving strain of the system (observed with GPS, tiltmeters, strainmeters) the model represents the short-term temporal evolution of the averaged energy of seismic radiations (observed as tremors and LFEs).

The rheological model is presented in section 2, together with its numerical scheme. Its implementation in an idealized shearing experiment that is relevant in the context of subduction zones is described in section 3. The main characteristic numbers and times describing this experiment are described in section 4. Section 5 presents a demonstration of its mechanical and numerical behaviour, with a sensitivity analysis on the value of its main parameters. This analysis demonstrates its capability to simulate the wide separation of scales between the brittle and ductile processes and transient deformations at the intermediate time scales.

2 The Physical Model

The model builds on the Burgers framework, which combines the Maxwell (an elastic and a viscous component in series) and the Kelvin-Voigt (an elastic and a viscous component in parallel) visco-elastic models (see figure 1). As mentioned in section 1.2, for the sake of the current paper we neglect the effect of the delayed elasticity of the mantle, which is responsible for instance for the reversal of surface velocities following major earthquakes but is probably of second-order in the context of slow earthquakes. In the following description, the model is therefore reduced to the Maxwell component. In particular, we focus on testing the capability of this component to reproduce transient

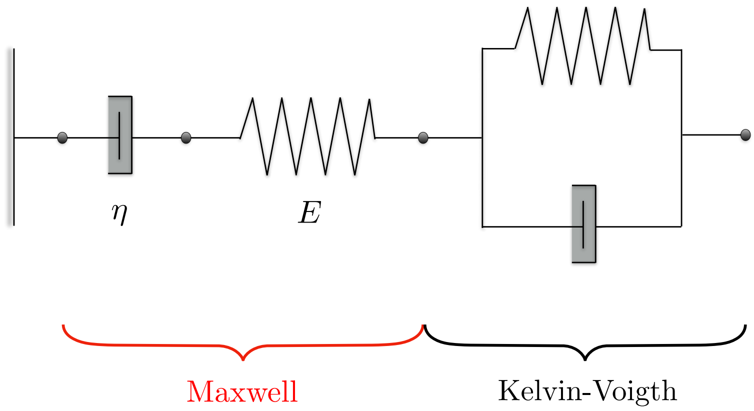

Figure 1. Schematic representation of the Burgers model. When loaded with a constant deformation, the Maxwell component undergoes a relaxation (exponential decay) of the stress. When unloaded, the part of the deformation associated to the viscous element is non-recoverable. When loaded with a constant stress, the Kelvin component leads to an exponential decay of the deformation. When unloaded, this deformation is fully recoverable. The implementation of the model described in this paper neglects the Kelvin component.

deformations and a deformation cycle akin slow earthquakes when E and η are not constant but allowed to evolve in both space and time, according to the local degree of fracturing of the material at the sub-grid scale, the so-called *level of damage*. The development of the current visco-elastic framework therefore lies crucially on the formulation of a coupling between E and η and this level of damage. The starting point of this coupling follows the simple formulation suggested by (Dansereau et al., 2016a), which was shown to successfully reproduce the spatial localization and intermittency of the damage and deformation and associated scaling laws in another quasi-brittle material that undergoes permanent deformations partially dissipating stresses when fractured; sea ice.

Another particularity of our approach is that, contrary to existing visco-elastic layered models (e.g., K. Wang et al., 2012; Sun & Wang, 2015), here a unique rheology is applied to the entire system (see figure 2). Its component are differentiated solely on the basis of the bulk elastic modulus and on the local level of damage.

2.1 Constitutive Equation

The Maxwell model is applied here in the context of an elastic, compressible solid. Its constitutive law reads

$$\frac{D\sigma}{Dt} + \frac{1}{\lambda}\sigma = E\mathbf{K} \colon \dot{\varepsilon}, \tag{1}$$

where $\mathbf{K}$ is the elastic stiffness tensor, defined in terms of Poisson's ratio, $0 \le \nu < 0.5$, and from which the elastic modulus, E, is factored out. For any three-dimensional symmetric tensor $\epsilon = \epsilon_{ij} \in i, j; 1 \le i, j \le 3, (\mathbf{K} \colon \epsilon)_{ij} = \frac{\nu}{(1+\nu)(1-2\nu)} tr(\epsilon)\delta_{ij} + 2\frac{1}{2(1+\nu)}\epsilon_{ij}$. The strain rate tensor, $\dot{\varepsilon}$ is taken equivalent to the rate of strain tensor and is given by $D(\mathbf{u}) = \frac{\nabla\mathbf{u} + \nabla\mathbf{u}^T}{2}$ where $\mathbf{u}$ is the velocity. The ratio of the material's apparent viscosity and elastic modulus, $\lambda = \eta/E$, hereinafter referred to as the relaxation time, sets the mesoscopic rate of dissipation of the stresses through permanent deformations.

Following Kachanov (1958) and previous isotropic damage models (e.g., Tang, 1997; Lyakhovsky, Ben-Zion, & Agnon, 1997; Amitrano et al., 1999) the density of cracks at the sub-grid scale is described by a mesoscopic scalar damage variable, d, the value of which evolves between 0 for an undamaged and 1 for a totally damaged material (see

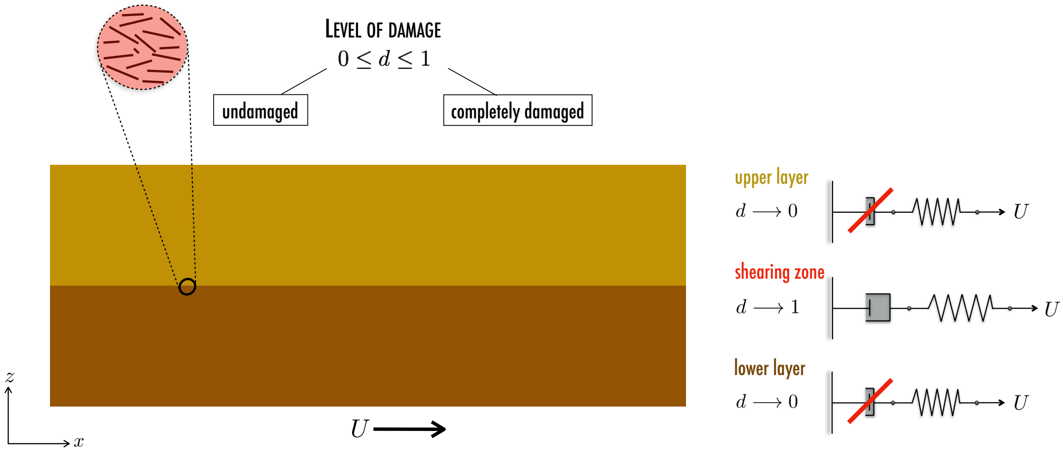

Figure 2. Schematic representation of the model and simulations, which represent a vertical (x, z) cross-section of two layers of host rock sheared by applying a constant velocity at the bottom of the lower layer, in the x-direction. A unique visco-elasto-brittle constitutive law is applied to the entire system. The two layers are differentiated only on the basis of the undamaged value of their elastic modulus. The expected mechanical behaviour is one in which the bulk of both layers is quasi-elastic, since damage there is expected to be almost zero and the effective viscosity is high, and visco-elastic at the interface of the two layers, where the deformation and damage are localized and potentially high and the elastic modulus and apparent viscosity much reduced.

figure 2). In the case of the elastic modulus, the coupling to d is based on the principle of effective stress (Kachanov, 1958) and reads

$$E = E_0(1 - d), \tag{2}$$

where E_0 is the undamaged elastic modulus of the material. In the case of the effective viscosity, η, the coupling reads:

$$\eta = \eta_0(1 - d)^{\alpha}, \tag{3}$$

where η_0 is the bulk viscosity of the material, i.e., its viscosity in its undamaged state, and α is an exponent > 1 such that the relaxation time, λ, setting the rate of dissipation of the stresses, decreases with the degree of fracturing of the material. This ad-hoc but simple coupling allows, on the one hand, the dissipation of the stress through permanent deformations where the material is damaged and, on the other hand, the conservation of the stress associated to elastic deformations where the material is relatively undamaged (Dansereau et al., 2016a; Weiss & Dansereau, 2017).

2.2 Progressive Damage Mechanism

The level of damage in the model evolves due to both fracturing and healing processes. The first of these processes translates into an increase in d and its occurrence is determined at any given model iteration by comparing the local state of stress to a critical stress value, set by a chosen damage criterion. The present implementation uses the Mohr–Coulomb criterion

$$\sigma_1 = q\sigma_2 + \sigma_c, \tag{4}$$

where σ_1 and σ_2 are the principal stresses, $q = \left[(\mu^2 + 1)^{1/2} + \mu\right]^2$, μ is the internal friction coefficient and $\sigma_c = \frac{2C}{\left[(\mu^2+1)^{1/2} - \mu\right]}$, where C is a non-zero cohesion (resistance of the material to pure shear). No truncation is applied here to this criterion in the case of $\sigma_1, \sigma_2 < 0$: hence it includes tensile stresses. In a manner similar to other damage modelling frameworks, some noise is introduced in this criterion, by drawing the value of C over each element of the discretized domain from a uniform distribution, to represent the heterogeneity of natural materials and insure progressive failure even under perfectly homogeneous forcing conditions.

As in the elasto-brittle model of (Amitrano et al., 1999), d evolves due to damaging following

$$1 - d' = \delta d \, (1 - d) \,, \tag{5}$$

where d' is the post-damaging value of damage, d, the pre-damaging value and δd, a constant multiplication factor such that $\delta d = 0$ when and where the state of stress is subcritical and $0 < \delta d \leq 1$ when and where it is over-critical with respect to the damage criterion. According to equations (2) and (3), each damage event implies that the local elastic modulus and apparent viscosity decrease respectively as

$$E' = \delta d E \tag{6}$$

$$\eta' = \delta d^{\alpha} \eta \tag{7}$$

where the superscript $'$ is hereinafter used to denote the post-damage strength, stress and deformation. This local decrease in mechanical strength leads to an elastic redistribution of the stresses from the over- to the sub-critical areas of the material, which allows for the triggering of avalanches of damaging events, representing the propagation of cracks at the mesoscale, as long as the elastic modulus (or relaxation time) or the material remains significant. It is important to note that, as other damage frameworks, the current model is not *dynamic* and as such, is not meant to capture the propagation of the rupture that generates seismic waves. Instead, it aims at representing the effect of such rupture processes on the deformation of the material.

In developing the model, we take advantage of the very large separation of scales between the brittle and ductile deformations in faults to make the assumption that the first type of deformation is quasi-instantaneous relative to the second type. As such, we treat the evolution of the level of damage as independent of time. The same approximation is implicitly made in the time-independent (linear) elasto-brittle brittle model of (e.g., Amitrano et al., 1999). Here, we therefore follow a similar approach and formulate a steady-state, iterative scheme for the stress redistribution associated with micro-fracturing and fracture coalescence at the sub-grid scale. This formulation relies on two hypotheses:

1. the *immediate* effect of damage is to redistribute the local stresses, not strains. In the following, this immediate post-damage state is referred to using the "*" superscript,
2. as the propagation of damage is quasi-instantaneous compared to viscous relaxation processes in the material considered, the viscous stress dissipation term in equation (1) can be neglected when solving for the damage propagation. The constitutive equation therefore reduces to that of a linear-elastic material:

   $$\sigma = E\mathbf{K} \colon \varepsilon,$$

   where ε is the deformation (as opposed to the deformation rate) tensor.

The following constitutive equations thereby define respectively the pre- and immediate post-damage states:

$$\sigma = E\mathbf{K} \colon \varepsilon,$$

$$\sigma^* = E^*\mathbf{K} \colon \varepsilon^*,$$

Using the first hypothesis laid above, the following equality relating the pre-damage and the immediate post-damage elastic modulus (respectively E and E^*) and stresses (σ and

σ^*) can be written

$$\frac{\sigma^*}{E^*} = \frac{\sigma}{E}.$$

Using equation (6), the immediate post-damage stress adjustment is therefore given by

$$\sigma^* = \sigma\delta d.$$

Considering further that this local stress adjustment induced by the damage event will lead, in a second time, to an adjustment in the neighbouring deformation and so, stress, the new state of equilibrium between the post-damage stress, σ', and the post-damage deformation, ε', is given by

$$\sigma' - \sigma\delta d = E_0(1 - d')\mathbf{K} : \varepsilon'. \tag{8}$$

2.3 Healing Mechanism

Healing is another essential ingredient for the reproduction of the deformation of fault zones (e.g., Bos & Spiers, 2002; Renard et al., 2000, and many others). In the case of damaged rocks and rock gouges, it can include various processes, like sintering (e.g., Hirono et al., 2020), cementing and sealing from dissolution-precipitation processes (e.g., Sibson, 1992; R. T. Williams, Mozley, et al., 2019), motion/diffusion of asperities and dislocations (e.g., Dieterich, 1979a, 1979b, and many others) and compaction (e.g., Hunfeld et al., 2020). In the current model, the respective effects of all of these processes are not differentiated but rather encapsulated into a single healing law that prescribes a decrease in the level of damage at a constant rate such that:

$$\frac{Dd}{Dt} = -\frac{1}{t_h}d, \; 0 \leq d < 1, \tag{9}$$

where t_h the healing time. Through their respective coupling to d, both the elastic modulus and apparent viscosity are therefore allowed to re-increase towards their bulk value after damage events : a behaviour that is consistent with observations of the evolution of seismic velocities (Li & Vidale, 2001; Brenguier et al., 2008). This very simple law, used here for the purpose of demonstrating the general impact of healing on the modelled mechanical behaviour, could be refined in more realistic implementations of the model (see section 11).

2.4 The Coupled Visco-Elasto-Brittle Model

The proposed model couples the time-independent treatment of the damage propagation with the time-dependant, visco-elastic Maxwell constitutive equation and the time-dependant evolution equation for healing. To do so, the complete system of equations is solved in three steps or subproblems (P):

($P1$) The full constitutive equation (1) is first solved together with the full momentum equation, boundary and forcing conditions (see section 3) and using the field of damage at the previous time step for a first estimate of the field of velocity and stress at the current time step. The field of stress is then compared to the local damage criterion.

($P2$) *If and only if* the stress locally exceeds the damage criterion, the forcing is paused and the macroscopic deformation of the simulated material is held constant. The model enters a steady-state subiteration in which (i) the level of damage, d, is adjusted to its post-damage value, d', (ii) equation (8) is solved for the adjusted state of stress, σ'. These two steps are carried iteratively until all states of stresses become sub-critical, at which point the stress state at the current time is set to the adjusted stress at the final subiteration.

($P3$) The healing equation (9) is solved for the field of damage at the current time step, using the post-damaging level of damage, d'.

This scheme is illustrated schematically in figure 3 and presented in full details in Appendix B.

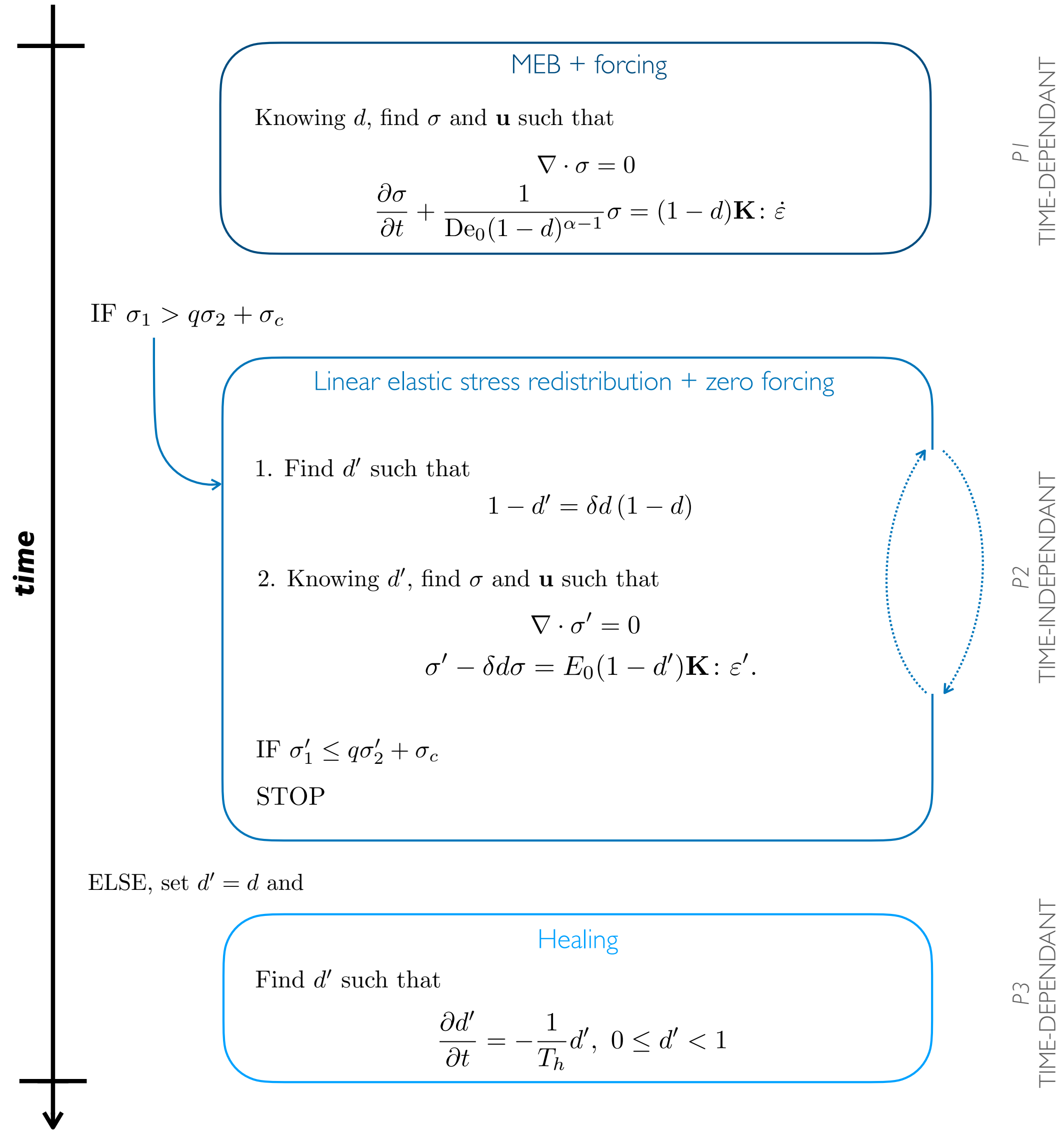

Figure 3. Schematic representation of the numerical scheme, composed of the three sub-problems, and its resolution over one model time step. For simplicity, the superscript '~' for adimensional variables is dropped. The full numerical scheme and time discretization is described in Appendix B.

3 Implementation

The model is implemented here in a 2-dimensional shearing experiment (see figure 4), meant as a very idealized representation of a vertical cut (x, z) through a subduction zone. Two layers of host rock are sheared by applying a constant $x-$ velocity

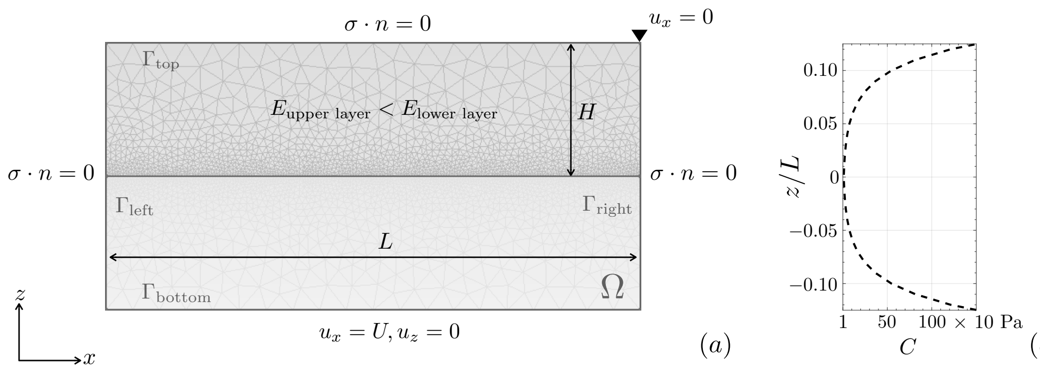

Figure 4. (a) Simulation setup. The domain, boundaries and boundary conditions are detailed in Appendix B. (b) Functional dependence of the cohesion, C, (i.e., of the damage criteria) on z, prescribed to avoid concentrating most of the deformation at the top and bottom boundaries, where the $x-$velocity is either locally or entirely prescribed.

at the bottom of the lower layer. No confinement is applied on the lateral sides and the surface is free, except for the top, right corner of the domain (the furthest surface point downstream and in the direction of the forcing), for which $u_x = 0$. The horizontal extent of the system perpendicular to the shearing direction is considered much greater than the horizontal extent in the shearing direction. Plane strains are therefore assumed. No discontinuity is introduced over the domain other than in the value of the undamaged elastic modulus, E_0, which is lower by a factor of 3 in the upper layer, representing the continental crust, than in the lower layer, representing the oceanic crust (see table 1). Also, in order to avoid that all of the deformation be trivially accommodated near the bottom boundary of the domain, where a non-zero $x-$velocity is prescribed, or near the top, right corner of the domain, where the $x-$velocity is fixed to 0, a functional dependence of C on z is prescribed, of the form $C = C_0 \times \exp(|5.0 * z/H|)$, where H is the thickness of both layers (see figure 4b) and C_0 is the minimum cohesion. This function allows the magnitude of C to vary little over a wide enough range of values of z centred on $z = 0$ (e.g., $C(z = 0.01) = 1.5 \times C(z = 0)$ and therefore does not affect the degree of localization of the deformation in the shearing zone that forms between the two simulated layers. Over each grid cell element, this function is locally multiplied by a value that is picked randomly over a uniform distribution of values over the range [0.75 1], thereby introducing some noise in the local damage criteria that represents the natural heterogeneity of the material (see section 2.2).

The balance of forces in the experiment neglects inertia and advection. In order to avoid introducing artifacts in the solution related to our finite-size domain and boundary conditions, we also neglect gravity. The momentum equation therefore reads:

$$\nabla \cdot \sigma = 0. \tag{10}$$

As slow earthquakes entail deformations (i.e., slip) that are relatively small relative to the horizontal and vertical extent of subduction zones, the advection, rotation and deformation terms which are included in material derivatives in the constitutive equation (1) and healing equation (9), are all neglected, such that $\frac{D\sigma}{Dt} = \frac{\partial \sigma}{\partial t}$ and $\frac{Dd}{Dt} = \frac{\partial d}{\partial t}$. In all simulations performed here, the total, cumulative deformation of the system remains below 10% of the the size of the smallest mesh element, ensuring that this approximation is indeed valid. The effect of the elastic deformations on the material's density are neglected as well, such that mass conservation does not need to be imposed.

Model/setup parameters		**Value**
Length of the domain	L	$10^6, 10^4, 10^2$ m
Thickness of both layers	H	$\frac{1}{8}L$
Tectonic forcing velocity	U	10^{-9} m s^{-1}
Undamaged relaxation time	$\lambda_0 = \frac{\eta_0}{E_0}$	10^{12} s
Poisson's ratio	ν	0.3
Internal friction coefficient	μ	0.7
Maximal cohesion	C_0	10^4 Pa

Table 1. Model and simulation parameter values.

The model equations are discretized in time using a backward Euler scheme of order 1 (see section B01 of the Appendix for the details) and discretized in space using finite elements. In the following, Δt designate the model time step and Δx, the spatial resolution of the mesh grid. The triangular elements grid used is built using the Gmsh generator (Geuzaine & Remacle, 2009). As the model is isotropic by construction, and in order to avoid preferential orientations in the localization of the deformation, it is chosen unstructured. The spatial resolution, Δx, is set to be 1/20 of the horizontal extent, L, of the domain at the top and bottom boundaries. It is refined by a factor of 10, so that to be 1/200 of L, at the junction of the two layers (see Figure 4) where deformation is expected to be maximal. As cumulative deformations are small in all simulations, the deformation of the mesh is not calculated and the position of grid nodes, not updated in time. The resolution of the variational formulation of the equations make use of the C++ library RHEOLEF (Saramito, 2020). The polynomial approximations for $\mathbf{u}$ are of order 1 and continuous at inter-element boundaries. As the stress tensor is a function of the velocity gradient and the damage, a function of the stress tensor, the approximations for σ, σ', d and d' are of degree 0 and discontinuous at inter-element boundaries.

4 Adimensional System of Equations and Adimensional Parameters

In all of the simulations performed here, the system of equations is solved and results are expressed in adimensional form. This allows describing and exploring the sensitivity of the rheological framework in terms of a reduced set of parameters and using the same idealized setup to represent systems with different physical dimensions and/or deformation time scales.

The model is made adimensional with respect to the horizontal extent, L, of the domain, the constant velocity prescribed at the bottom of the lower layer, U, and the average of the undamaged elastic modulus of the two layers, E_0. The time, T, characterizing the deformation process is therefore given by $\frac{L}{U}$. The superscript '$\tilde{}$' is used for all dimension-less variables and operators, which are listed in table A1. For a full description of the adimensional formulation of the variables and equations, the reader can refer to Appendix A.

The complete adimensional system of equations reads

$$
\begin{aligned}
\tilde{\nabla} \cdot \tilde{\sigma} &= 0 && (11)\\
\frac{\partial \tilde{\sigma}}{\partial \tilde{t}} + \frac{1}{\mathrm{De}_0 (1-d)^{\alpha-1}} \tilde{\sigma} &= (1-d)\mathbf{K} : \tilde{\dot{\varepsilon}}, && (12)\\
1 - d' &= \delta d \, (1-d) && (13)\\
\tilde{\nabla} \cdot \tilde{\sigma}' &= 0 && (14)\\
\tilde{\sigma}' - \delta d \tilde{\sigma} &= (1-d')\mathbf{K} : \tilde{\varepsilon}' && (15)\\
\frac{\partial d'}{\partial \tilde{t}} &= -\frac{1}{T_h} d', \; 0 \leq d' < 1, && (16)
\end{aligned}
$$

with the damage criterion

$$\tilde{\sigma_1} = [(\mu^2+1)^{1/2} + \mu]^2 \tilde{\sigma_2} + \frac{2C/E_0}{[(\mu^2+1)^{1/2} - \mu]}. \quad (17)$$

The value of Poisson's ratio, ν, and of the internal friction coefficient, μ, are fixed in the following simulations to values common for geomaterials (Byerlee, 1978; Jaeger & Cook, 1979). The brittleness of the material, given by the ratio of the cohesion to the undamaged elastic modulus, C_0/E_0, is also kept constant. Besides these parameters, the four adimensional parameters that characterize the model are:

1. $\mathrm{De}_0 = \frac{\eta_0}{E_0} \frac{U}{L}$, the (undamaged) Deborah number,
2. α, the damage parameter, setting the rate at which the viscosity (or relaxation time) decreases with the level of damage,
3. δd, the damage increment,
4. $T_h = \frac{t_h}{T}$, the time for healing,

The limits and range of values over which these parameters are varied in the sensitivity experiments performed here are summarized in Table 2 and discussed in the following sub-sections.

Adimensional parameter		**Range of values**
Characteristic healing time	T_h	$10^{-1} - 10^{-7}$
Undamaged Deborah number	De_0	0.01, 0.1, 10
Damage increment	δd	$0.1, 0.3, 0.5, 0.7, 0.9$
Damage parameter	α	$2, 3, 4, 6, 8$

Table 2. Adimensional model parameters and the range of values over which they are varied in the model sensitivity experiments.

4.1 The Deborah Number, De

The Deborah number can be defined as the dimensionless ratio of the viscous relaxation time for the stress, λ, and of the time for the deformation process, $T = \frac{L}{U}$, (i.e., the inverse of the macroscopic shearing rate). It characterizes the fluid-like versus elastic solid-like behaviour in unsteady flows, and as such is a relevant quantity to characterize the deformation of faults and the slow earthquake phenomenon. Materials characterized by a low Deborah number, either because they dissipate stresses rapidly or because they are deformed very slowly, have a behaviour that approaches that of a (Newtonian) fluid and therefore flow steadily. Materials characterized by a high Deborah number, either because they dissipate stresses very slowly or because they are deformed rapidly, behave like elastic solids and flow unsteadily.

Compared to classical earthquakes, slow earthquakes appear to be a less intermittent, or equivalently a more steady, and therefore a more predictable form of deformation. Indeed, in some subduction zones like Cascadia (Dragert et al., 2001) and Guerrero, Mexico (Cotte et al., 2009; Radiguet et al., 2012) major slow earthquake episodes show approximately stable recurrence times. However, the recurrence interval of slow slip events varies greatly from one subduction zone to another. For instance, it is of a few months in some segments of the Nankai subduction in Japan (e.g., Poiata et al., 2021), on the order of one year in Cascadia, and of nearly four years in Guerrero. Recurrence interval are also known to differ for different segments of the same subduction zone (e.g., Brudzinski & Allen, 2007) and are observed to decrease with depth (e.g., Wech & Creager, 2011; Frank, Radiguet, et al., 2015).

To take into account this variability in our simulations, as well as the variability and uncertainty related to the mechanical properties of the crust (elastic modulus and viscosity), we explore three values of the *undamaged* Deborah number (0.001, 0.1 and 0.1, see table 3) each separated by two orders of magnitude. Practically, in the simulations, these different values are obtained by varying the time associated with the deformation process, $T = \frac{L}{U}$, and maintaining the undamaged relaxation time, $\lambda_0 = \frac{\eta_0}{E_0}$, constant ($\lambda_0 = 10^{12}$ s). This relaxation time is consistent with an undamaged elastic modulus, E_0, on the order of 10^{11} Pa (in agreement with e.g., Dziewonski & Anderson, 1981) and a bulk, undamaged viscosity, η_0, of 10^{23} Pa s (Siravo et al., 2019) for both the continental and oceanic crust. The deformation process time, T, is set by considering a typical tectonic velocity of 10^{-9} m/s (on the order of a few cm/year) and considering different horizontal extent, L, over which the fault is activated and slip occurs. The lowest value of De_0 explored considers $L = 10^6$ m (1000 km), representative of a large subduction zone. Following the definition of the Deborah number, this lower bound can be interpreted alternatively as representing a smaller but deeper, hence lower viscosity segment of a fault. The highest value is representative of a small activated segment (1000 m) or alternatively, as a larger but shallower and hence more brittle part of a fault.

It is very important to note, however, that while De_0 sets the bulk fluid-like versus elastic solid-like behaviour of the system and therefore is a relevant quantity to characterize the macroscopic deformation cycle, for instance in terms of its duration, in the visco-elasto-brittle model presented here, the *effective* Deborah number, De, is not homogeneous throughout the system but varies in space and time. Indeed, according to equations (2) and (3), De evolves locally as a function of the level of damage, as $\mathrm{De} = \mathrm{De}_0 d^{\alpha-1}$. In all three systems, this decrease will leads to a more fluid-like behaviour where and when the host rock becomes damaged.

4.2 The Healing Time, T_h

In the present model, the healing time represents the time it takes for a completely damaged element ($d = 1$) to evolve back to its undamaged state ($d = 0$) and recover entirely its mechanical strength. Since several different healing processes are thought to be at play in faults (see section 2.3) and the rates at which these different processes very likely depend on various local factors, like pressure, temperature, the availability of fluids and the type of rock (see for instance McLaskey et al., 2012), estimating T_h is highly non-trivial. Therefore, we define our estimation here based on lower and upper bounds values. On the one hand, observations of post-seismic velocity changes, which estimates the time required for the velocity of P and S waves (or, by extension, the elastic modulus of the crust in the vicinity of the fault) to re-increase to their pre-seismic value, place the lower bound to a few (2-5) years (e.g., Li et al., 1998; Brenguier et al., 2008). Indeed, while cracks that open during the mainshock probably close partially with time, one still expects the vicinity of the shearing zone to remains highly damaged relative to the surrounding host rock and that, at all times. On the other hand, assuming that the fault heals completely between large earthquakes, the upper bound can be estimated from pseudo-recurrence times, which reach a few thousand years in some faults (e.g., Li et al., 1998; R. T. Williams, Davis, & Goodwin, 2019).

Four orders of magnitude of healing time are explored here, which vary between these lower and upper bounds. In dimensional form, these values are: $t_h = 10^8$ s, which is equivalent to about $\sim$ 3 years, 10^9 s ($\sim$ 30 years), 10^{10} s ($\sim$ 300 years) and 10^{11} s ($\sim$ 3000 years). Since different De_0 numbers are explored by varying the process time T, and as time in our system of equations is made adimensional with respect to T (see section 4), the different De_0 lead to different adimensional values of the time of healing, T_h. The dimensional and corresponding adimensional values of t_h and T_h corresponding to each De_0 are listed in table 3.

4.3 The Damage Parameter, α

As mentioned in section 2.2, the purpose of the rather "ad-hoc" damage parameter, α, is that the model accounts for a more rapid dissipation of the stresses where the material is highly damaged than where it is relatively undamaged. The only physical constraint on its value is therefore $\alpha > 1$. There is no theoretical upper bound for α. However, for α large, the relaxation time becomes very small at the onset of damage, whatever the damage level. Dansereau (2016b) and Weiss and Dansereau (2017) have demonstrated that in this case, stresses are readily dissipated after each damage event and the mechanical behaviour becomes essentially elasto-plastic. Here, the sensitivity of the model is investigated for values of α between 2 and 8, which proves to be a wide enough range of values for the model to exhibit different mechanical behaviours relevant in the context of faults and slow earthquakes.

4.4 The Damage Increment, δd

Similar to the damage parameter, the value of the damage increment is not constrained other than within the range of values intrinsic to its definition : between 0 and 1. It is however expected to be determinant on the mechanical response of the model. For large values of δd, the decrease in E at each damage event, given by equations (6) and (7) respectively, as well as the associated increase in the level of damage, given by equation (5), are small. Conversely, for small values of δd, the decrease in E and η and associated increase in d at each damage event is large. In the first limit, the dissipation of the stress in permanent deformations is small. One can expect the emergence of a brittle creep regime, in which the system remains always near criticality. In the second limit, the dissipation of the stress into permanent deformations is large, which can impede elastic interactions in the system and, by the same fact, the spatial and temporal localization of the deformation (Dansereau, 2016b; Weiss & Dansereau, 2017). In the following, the model behaviour is analyzed for damage increment values of 0.1, 0.3, 0.5, 0.7 and 0.9.

5 Results

5.1 Mechanical Model Response

Here we first describe the overall macroscopic behaviour of the model. This description is based on simulation results obtained for a specific set of model parameters ($\mathrm{De}_0 = 0.001$, $T_h = 10^{-5}$, $\tilde{\Delta t} = 10^{-10}$, $\alpha = 4$, $\delta d = 0.1$), but the conclusions broadly apply to a wider range of values. Figure 5a shows the temporal evolution of the model response in terms of the macroscopic shear stress, calculated by integrating the shear stress on the entire top boundary of the domain, and of the *macroscopic damage increment*, de-

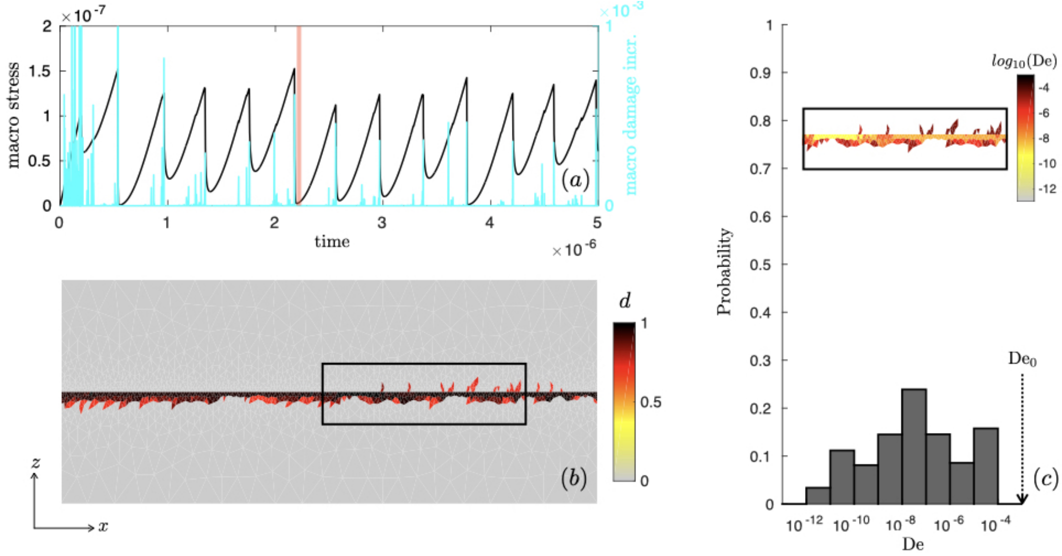

Figure 5. (a) Temporal evolution of the macroscopic shear stress (black line) and of the macroscopic damage increment (as defined by eq. 18, cyan line) for a simulation using $\mathrm{De}_0 = 0.001$, $\tilde{\Delta t} = 10^{-10}$, $\alpha = 4$, $\delta d = 0.1$ and $T_h = 10^{-5}$. (b) Instantaneous field of the level of damage after the large avalanche of damage events and associated unloading phase indicated by the vertical red line on panel (a). (c) Zoom-in on the instantaneous field of De (in logarithmic scale) corresponding to the black box indicated on panel (b) and normalized distribution of the instantaneous values of De for all damaged elements of the domain corresponding to the unloading phase indicated by the vertical red line on panel (a).

fined as the local damage increment integrated over all elements I that are damaged during a stress redistribution subiteration k and over the K subiterations realized over the current model time step, $n+1$:

$$\sum_{k=1}^{K}\sum_{i=1}^{I}(1-\delta d)(1-d_i^{n,k}). \tag{18}$$

An animation of this simulation, showing the temporal evolution of the field of damage (in logarithmic scale) and of both the macroscopic shear stress and damage increment is available as Supporting Information to this paper (see S1). After the initial and almost linear-elastic loading phase, this response is characterized by asymmetric cycles comprised of an either partial or total stress drop (hereinafter called unloading phase) and a subsequent healing and stress increase phase (hereinafter called loading phase). Damage can occur at any moment of the cycle, but unloading phases are generally characterized by the largest avalanches of damaging events, which can span either a large part of or the entire domain (see S1). When the stress drop is partial, it is generally comprised of an initial brutal drop associated to a large damage avalanche, followed by a slower relaxation phase, not necessarily associated to significant further damage. This post-rupture, or "post-seismic", relaxation results from viscous-like permanent deformations along a fault made of highly damaged, hence low viscosity, material. Such behaviour is made possible by the rheology proposed above. The occurrence of pre-rupture (akin to foreshocks) or post-rupture (akin to aftershocks) damage events varies with the choice of model parameters (see section 11 below). However, for all simulations and parameter values covered here, the damaging activity localizes at the interface of the two layers (mostly within the lower plate, see figure 5b), a behaviour that is not prescribed but that arises naturally due to the forcing condition applied at the bottom of the lower layer and to the small difference in elastic modulus assigned to each layer. Consequently, the deformation of the system is also highly localized at this interface. Figure 5b also indicates that damage is heterogeneously distributed along the interface. As a consequence of the prescribed coupling between d and both the E and η (see eq. 2 and 3), this heterogeneity in damage leads to a large heterogeneity in the value of the relaxation time, or equivalently of the effective De number, along the interface. As indicated by the distribution shown in Figure 5c, the values of De associated with damaged grid elements indeed span several orders of magnitude. The lowest values of De are obtained at the end of unloading phases and re-increase as the system heals towards the end of loading phases.

However, it is worth noting that, over the range of parameter values explored here, the vicinity of the interface remains relatively highly damaged at all times (see S1) and never completely heals: a behaviour that is expected in the context of active faults. By the same fact, and because the simulations are initialized from a uniformly undamaged state ($d = 0$ everywhere), the behaviour during the first loading-unloading cycle is very different from the subsequent ones : the damaging activity is relatively much higher because the damaged zone is created from scratch while over all subsequent cycles, the interface is already damaged to a relatively large degree. In all further analyses of the model behaviour, this first loading-unloading cycle is therefore discarded.

5.2 Convergence and Numerical Efficiency

Here we verify that the macroscopic behaviour of the model converges with increasing temporal resolution. To do so, for the three identified values of De_0 (see section 4.1), simulations are run with five different values of the (adimensional) time step, $\tilde{\Delta t}$. All of these simulations use the same value of the damage increment ($\delta d = 0.1$) and of the damage parameter ($\alpha = 4$) and are initiated with the same field of noise on the cohesion. We explored a range of values of the healing time for these simulations, and retained the one value that produced the most physically sound results for each set of simulations with a given De_0 value (see section 5.3.1).

Figure 6 shows the temporal evolution of the model response in terms of the macroscopic stress (a) and of the macroscopic damage increment (b), defined as in eq. (18). It indicates that the largest value of the time step explored here leads to a pathological model response. This is expected, as this $\tilde{\Delta t}$ value approaches the order of magnitude of the main period of the loading-unloading cycles : this temporal resolution therefore does not allow resolving the progressive propagation of the damage in the system, nor the sharp stress drop associated with each macroscopic rupture. For smaller values of the time step, the model response converges well in terms of the main frequency and amplitude of the macroscopic stress variations when increasing the temporal resolution. It is also the case for the macroscopic variations in the deformation of the system (not shown) and in the damage increment.

To robustly test the convergence of the model response, we use a single metric that combines these three different pieces of information : the local damage increments and the resulting redistribution of the stress and of strains over the entire system. This is the elastic energy released within the system due to the propagation of damage, E_{brit}, the temporal evolution of which is shown in figure 6c. The distribution of this energy can be directly related to that of acoustic emissions associated to the micro-fracturing of rocks (e.g., Amitrano, 2003) and can therefore serve as a proxy for the seismic signal recorded at the geophysical scale. At each current (n+1) model time step, E_{brit} is estimated as

$$E_{brit}^{(n+1)} = \sum_{i=1}^{I} \frac{A_i}{A_{tot}} \left(\sigma_i^{(n+1,0)} : \varepsilon_i^{(n+1,0)} - \sigma_i^{(n+1,K)} : \varepsilon_i^{(n+1,K)} \right), \tag{19}$$

where i designate each element, I, the total number of elements over the domain, A_i the area of each element and A_{tot}, the area of the entire domain. The superscripts $n + 1, 0$

and $n+1, K$ refer respectively to the stress and strain values before and at the end of the avalanche of damaging events, which takes a total of K stress redistribution subiterations. To compare simulations using different time steps, E_{brit} is normalized by $\tilde{\Delta t}$. In agreement with the observed convergence in the variations of the macroscopic stress, deformation and damage increment, figure 6d clearly shows that the shape of the probability density function (PDF) of the normalized E_{brit} stabilizes over the three smallest values of time step explored here.

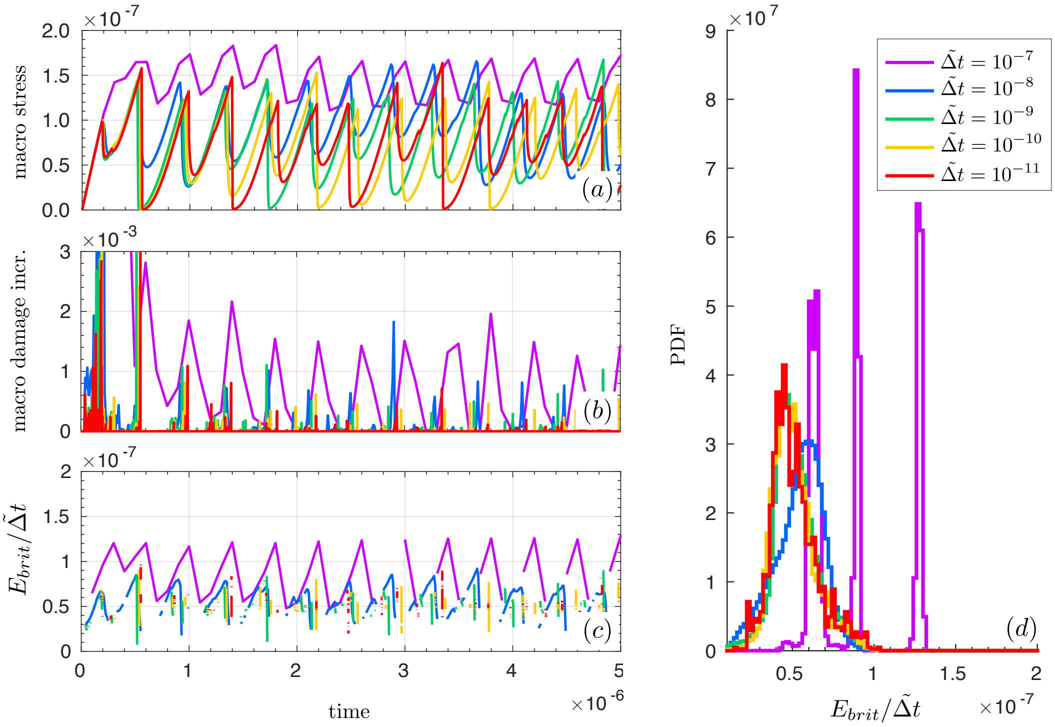

Figure 6. Temporal evolution of (a) the macroscopic stress, (b) the macroscopic damage increment and (c) the macroscopic elastic energy released due to the propagation of damage within the system, normalized by the time step $\tilde{\Delta t}$, for simulations using $\mathrm{De}_0 = 0.001$, $\alpha = 4$, $\delta d = 0.1$, $T_h = 10^{-5}$ and $\tilde{\Delta t} = 10^{-11}, 10^{-10}, 10^{-9}, 10^{-8}, 10^{-7}$ (corresponding to $\Delta t = 10^4$ s, 10^5 s, 10^6 s, 10^7 s, 10^8 s) (d) Probability density function of $E_{brit}/\tilde{\Delta t}$.

Simulations ran with $\mathrm{De}_0 = 0.1$ and $\mathrm{De}_0 = 10$, the same values of δd (0.1) and of the damage parameter, α, (4) and values of healing time of $T_h = 10^{-4}$ and $T_h = 10^{-3}$ respectively show that a similar convergence is retrieved in both cases over a range of values of $\tilde{\Delta t}$ (see figure C1 of Appendix C). These values are summarized in table 3: the red ones indicating a non-converged model response. The comparison of these values across the three De_0 explored here suggests that the time step should be chosen such that $\frac{\Delta t}{T} \lesssim 10^{-8}$ to ensure a fully converged and therefore physically meaningful model behaviour. The time step values corresponding to each De_0 value and retained for the sensitivity analyses on the other model parameters are indicated in green in table 3.

We further compare the simulations presented in figure 6 in terms of CPU and real simulation time. Each simulation was ran for a fixed (adimensional) total time of $5.0 \cdot 10^{-6}$, which represents, in dimensional equivalent, 160 years of evolution of the system. With the specific choice of model parameters employed in this particular simulation, each loading-unloading cycle covers about 12 years. The model response converges for time

T (s)	De_0	Δt (s)	$\tilde{\Delta t}$	t_h (s)	T_h
10^{15}	0.001	10^4	10^{-11}	10^8	10^{-7}
		10^5	10^{-10}	10^9	10^{-6}
		10^6	10^{-9}	10^{10}	10^{-5}
		10^7	10^{-8}	10^{11}	10^{-4}
		10^8	10^{-7}		
10^{13}	0.1	10^3	10^{-10}	10^8	10^{-5}
		10^4	10^{-9}	10^9	10^{-4}
		10^5	10^{-8}	10^{10}	10^{-3}
		10^6	10^{-7}	10^{11}	10^{-2}
		10^7	10^{-6}		
10^{11}	10	10^2	10^{-9}	10^8	10^{-3}
		10^3	10^{-8}	10^9	10^{-2}
		10^4	10^{-7}	10^{10}	10^{-1}
		10^5	10^{-6}	10^{11}	10^0
		10^6	10^{-5}		

Table 3. Values of the deformation timescale, T, the model time step, Δt, and healing time, t_h, explored in the present sensitivity experiments, with their adimensional counterpart : respectively, De_0, $\tilde{\Delta t}$ and T_h. For each value of De_0, the values of Δt (or $\tilde{\Delta t}$) for which the model response is not fully converged are indicated in red. The value of Δt (or $\tilde{\Delta t}$) retained for the sensitivity analyses on T_h, δd and α is indicated in green. For each De_0 value also, the optimal value of t_h (or T_h) retained for the sensitivity analyses on α and δd are indicated in green.

step values of $\tilde{\Delta t} = 10^{-11}, 10^{-10}$ and 10^{-9} (or $\Delta t = 10^4$, 10^5 and 10^6 s), which are equivalent to about $1/10, 1$ and 10 days respectively. For these three time steps, and for the spatial resolution described in section 3, the calculated CPU time is of about 25, 3 and 0.4 hours respectively (see figure 7). Considering that each simulation ran sequentially on a personal DELL computer equipped with 2.40 GHz Intel Xeon processors, these computational times demonstrate that the present numerical scheme makes it possible to run long-term simulations in the context of faults that cover several loading-unloading cycles in very reasonable simulation times. It is also interesting to note that, for the same three time steps for which convergence of the macroscopic model response is obtained, the calculated CPU time scales linearly with $\frac{1}{\tilde{\Delta t}}$, while it does not scale linearly for larger time steps ($\tilde{\Delta t} > 10^{-9}$). This indicates that for the smallest three $\tilde{\Delta t}$ values, the number of steady-state stress redistribution subiterations performed at each time step is nearly constant and hence does not depend on the model time step. Conversely, for larger $\tilde{\Delta t}$'s, the system is driven further out of equilibrium at each time (i.e., deformation) increment. The number of subiterations required for the stresses to be redistributed over the domain and to become sub-critical again then increases significantly with $\tilde{\Delta t}$, thereby reducing the gain in computational time.

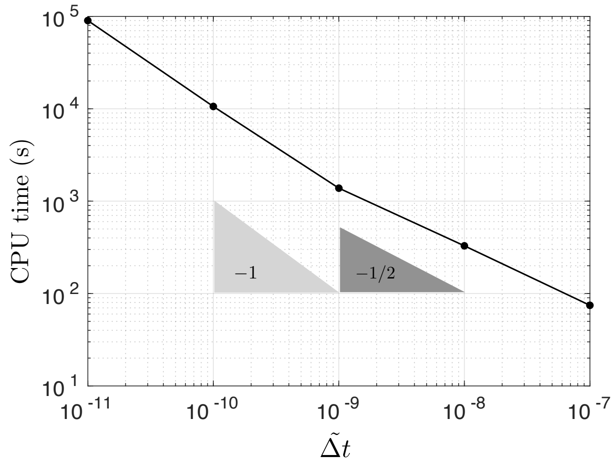

Figure 7. CPU time as a function of the (adimensional) model time step, for simulations using $\mathrm{De}_0 = 0.001$, $\alpha = 4$, $\delta d = 0.1$, and $T_h = 10^{-5}$ (see figure 6). Each simulation ran on a single (2.40 GHz Intel Xeon) processor on a personal DELL computer.

5.3 Sensitivity Analyses

5.3.1 Healing Time, T_h

To investigate the effect of healing in the model, we compare the macroscopic stress-strain time series and the power spectral density (PSD) of the elastic energy released within the system during the propagation of damage, E_{brit} (see figure 8), for simulations using $\mathrm{De}_0 = 0.001, 0.1$ and 10 and four different values of the time for healing, corresponding to dimensional times of $t_h = 10^8$ s, 10^9 s, 10^{10} s and 10^{11} s. All simulations use $\alpha =$ 4 and $\delta d = 0.1$ and a value of the time step that ensures the convergence of the model response for each De_0 value (see table 3). To account for the adjustment of the system following the first rupture, the first loading-unloading cycle is discarded when computing the PSD. Each curve shown on figure 8 is the average of 5 PSDs, on which a running mean centred over a window of 5 frequency values is applied.

The results clearly indicate that the prescribed time of healing controls the frequency of the loading-unloading cycles in the model: the larger the healing time, the lower the frequency. However in all of the simulations analyzed, the frequency associated to the prescribed healing time, indicated by the vertical lines on figure 8, does not correspond to the frequency of the loading-unloading cycles, but is systematically one or several orders or magnitude lower. This discrepancy is consistent that the interface always remains relatively highly damaged (see animation in Supporting Informations): less time is therefore required to re-initiate an avalanche of damaging events than it would be necessary if the system had completely heal. The discrepancy increases with the value of De_0, in agreement with a more elastic behaviour at high De_0 number, i.e. a lower contribution from viscous dissipation that delays the reloading of the system.

Another tendency in the model behaviour emerges. For all values of De explored here, large values of the healing time (slow healing) lead to a E_{brit} release, or equivalently a damaging activity, that concentrates around a narrow range of low frequencies: the PSD is therefore flat for high frequencies. The corresponding stress-strain curves indicates that the stress is very rapidly and completely dissipated at each unloading (damaging) event. This behaviour can be explained by the fact that these large values of healing time approach the value of the bulk relaxation time (i.e, the relaxation time of undamaged elements, or De_0). Healing is therefore too slow relative to the dissipation of the stress to play a significant role in the dynamics of the system.

Conversely, for low values of the healing time (fast healing), the PSD is flat for low frequencies, with the activity concentrated around a narrow range of high frequencies, and the stress is very rapidly but only partially dissipated at each damaging event: healing dominates the dynamics as T_h approaches the value of the relaxation time for the stresses over the most damaged elements in the system (i.e., De_{min}). This value tends to decrease inversely to T_h, as indicated by the coloured dotted lines on figure 8b.

For intermediate values of T_h and the two lowest values of De explored here (see figure 8a to d), the slope of the PSDs indicates the presence of correlations in the temporal evolution of E_{brit} (or, by extension, of the damaging activity). Such temporal correlation or clustering is systematically observed for seismic tremors in subduction zones and covers large spectrum of time scales, from hours to years (e.g., Idehara et al., 2014; Frank et al., 2016; Poiata et al., 2021). Therefore, for each investigated De value, we identify an "optimal" healing time as the value of T_h for which these correlations span the largest range of frequencies. It is important to note however, that the frequency at which spatial correlations emerge in the system is upper bounded in all simulations due to the finite dimension of the domain and the spatial resolution of the mesh. An intrinsic minimum time required to load the system can indeed be estimated, that depends only on the mechanical strength (the ratio C_0/E_0) and the spatial discretization of the model. It corresponds to the time it takes to load an initially undamaged system until the first damage event occurs, if all of the deformation is accommodated over a single single grid element. Figure 8b shows that the frequency associated to this time, indicated as $\frac{1}{t_{loading}}$ indeed marks the transition to a flat PSD at higher frequencies (for the other two systems, the time step employed is too large and does not allow exploring the model behaviour up to this frequency). For the "optimal" T_h values, corresponding to $t_h = 10^{10}$ s for $\mathrm{De} = 0.001$ (figure 8a, b blue curve) and $t_h = 10^9$ s for $\mathrm{De} = 0.1$ (figure 8c, d green curve), the times associated with the loading, the relaxation of the stresses over damaged elements and the healing of these elements are such that the three processes interact and give rise to temporal correlations in the system that span a wide range of time scales. Interestingly, the stress-strain behaviour of the model in these cases is characterized by loading-unloading cycles in which the stress is sometimes partially and more gradually dissipated and sometimes completely and drastically dissipated.

The optimal value of T_h decreases as the value of De_0 increases, indicating that systems that are more elastic-solid like (large relaxation time, λ) or characterized by a faster dynamics (small deformation time, $\frac{L}{U}$, either due to a small horizontal extent, L or a fast loading velocity, U) must encompass faster healing mechanisms for these interactions to take place.

However, for the largest De value used here (see figure 8e, f), temporal correlations in the damaging activity are restricted to a small range of time scale and that, for all of the T_h values explored, which we consider as lying in a realistic range in the context of faults. The associated macroscopic stress-strain behaviour is characterized by regularly-spaced, almost instantaneous (as opposed to transient) and complete unloading phases, akin to the stick-slip behaviour observed in block-slider experiments. In the context of slow earthquakes, this suggests that fault systems that are either very brittle (as near the surface), small in extent, or loaded too rapidly cannot host the complex spatio-temporal interactions that give rise to the observed transient deformations.

In the remaining sensitivity experiments (next section), we therefore leave the case of $\mathrm{De} = 10$ aside and concentrate on simulations using $\mathrm{De} = 0.001$ and $\mathrm{De} = 0.1$. The optimal values of T_h identified for these two cases are indicated in green in table 3 and used by default in all simulations.

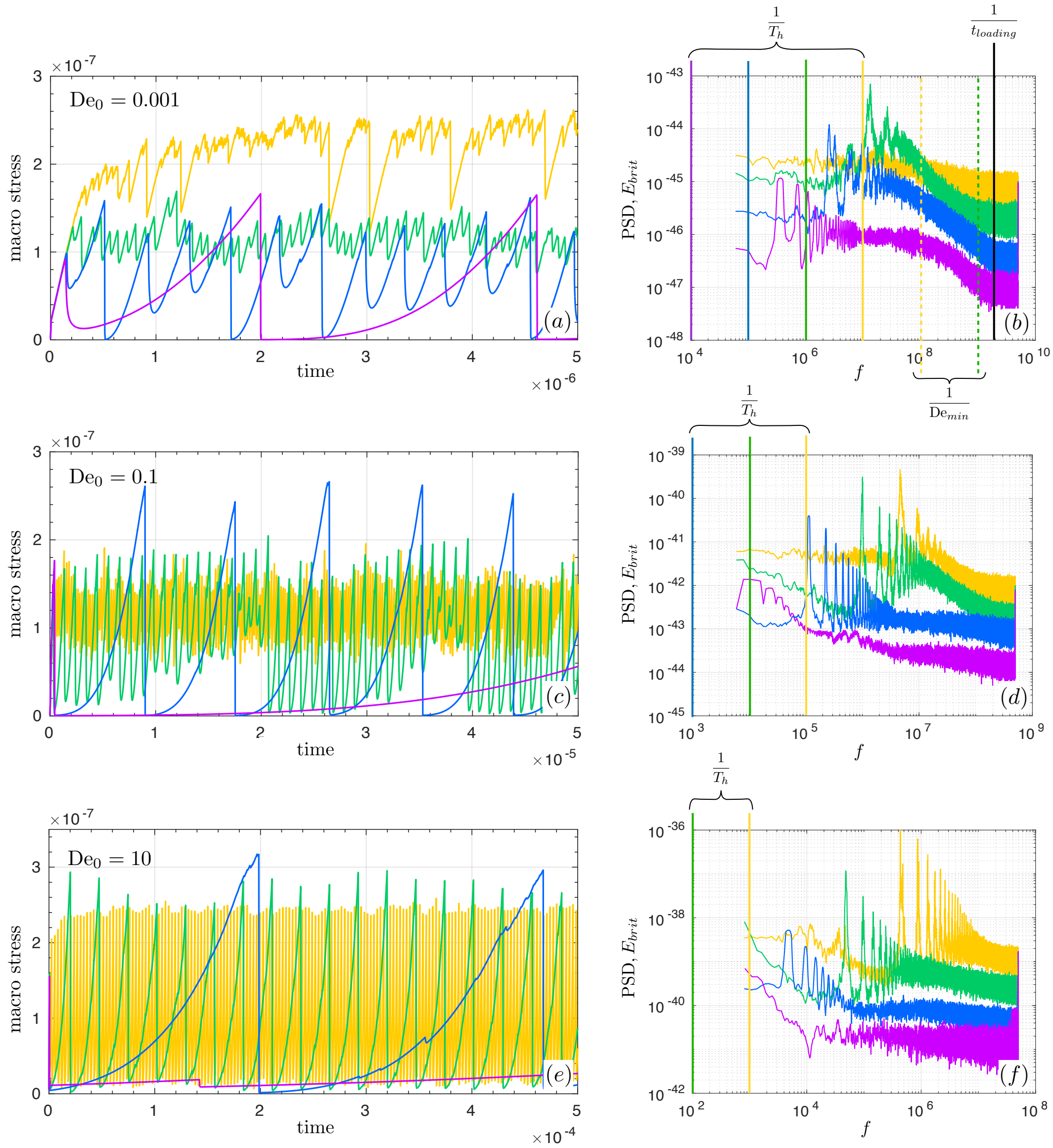

Figure 8. (a, c, d) Time series of the macroscopic stress and (b, d, f) power spectral density of the E_{brit} time series for simulations using (a, b) $\mathrm{De}_0 = 0.001$ ($\tilde{\Delta t} = 10^{-10}$), (c, d) $\mathrm{De}_0 = 0.1$ ($\tilde{\Delta t} = 10^{-9}$) and (e, f) $\mathrm{De}_0 = 10$ ($\tilde{\Delta t} = 10^{-8}$) and four adimensional values of the prescribed time of healing, corresponding to dimensional values of $t_h = 10^8$ s (yellow), 10^9 s (green), 10^{10} s (blue) and 10^{11} s (purple curve). All simulations use $\alpha = 4$ and $\delta d = 0.1$. Each PSD curve is an average of 5 PSD calculated for 5 simulations initiated with different realizations of the noise on C and on which a running mean centred over a window of 5 frequency values is applied. The vertical lines on the PSDs indicate, when these frequencies fall within the range of frequencies covered in the simulations, the frequencies associated with the four adimensional values of the prescribed time of healing, $1/T_h$ (plain coloured lines), the minimum time required to load the system, $1/t_{loading}$ (plain black line), and the relaxation time associated with the most highly damaged elements in the system, $1/\mathrm{De}_{min}$ (dashed coloured lines).

5.3.2 Damage Parameter, α, and Damage Increment, δd

The last set of sensitivity experiment focuses on the brittle versus ductile character of the model behaviour. As the parameters α and δd both regulate the rate at which the mechanical strength decreases locally and the behaviour changes from elastic solid-like and viscous fluid-like as a function of the level of damage, we expect their effect in this regard to be closely related. We therefore run a set of sensitivity experiments in which both parameters are varied simultaneously. The results of these experiments for the case of $\mathrm{De}_0 = 0.001$ ($\tilde{\Delta t} = 10^{-10}$ s and $T_h = 10^{-5}$ s) and $\mathrm{De}_0 = 0.1$ ($\tilde{\Delta t} = 10^{-9}$ s and $T_h = 10^{-4}$ s) are presented here.

We recall that for large values of δd, the local decrease in the elastic modulus, E, and apparent viscosity, η, at each damaging event is small. Conversely, for small values of δd, the local decrease in both E and η is large. Small values of α lead to a small decrease in the relaxation time, $\frac{\eta}{E}$, at each damaged element (the damaged material retains stresses longer), while large values of α lead to a large decrease in $\frac{\eta}{E}$ (stresses are dissipated more readily).

Damage Increment, δd

Time series of the macroscopic stress (see figure 9 and 10, left panels) show that for all values of α, increasing δd decreases the amplitude of the macroscopic stress drop associated with each unloading phase. As the stress is then never completely released at each loading-unloading cycle but stabilizes around a non-zero value, the loading time required for critical values of stress to be reached is reduced and the frequency of each cycle is thereby increased. For large values of δd, the PDF of the macroscopic damage increment, defined as in equation (18), is a truncated power law that is confined to small values of damage increment (see figure 9, right panels, which indicates that damage and deformation take place through isolated events, with small spatial extents.

Conversely, as δd is decreased, the amplitude in the variations of the macroscopic stress and the length of the loading-unloading cycles is increased. The unloading phases are characterized by sharper stress drops, indicating a more brittle behaviour. The distributions of the macroscopic damage increment are shifted towards larger values of damage increments.

Damage Parameter, α

For a given value of δd, increasing the value of α also induces larger macroscopic stress drops, lower frequency loading-unloading cycles and larger values of the macroscopic damage increment. Another effect of increasing α is that the stress relaxation and re-increase in the vicinity of each stress minimum is more progressive in time, consistent with a more rapid decrease in the viscosity of the material at the onset of damaging and a more viscous fluid-like, i.e, dissipative, behaviour. The inverse is true when decreasing α: the macroscopic behaviour is more brittle-like, with smaller but quasi-instantaneous stress relaxation phases and rapid, quasi-elastic stress loading phases.

Limit Cases

For virtually all values of α, large values of δd give rise to a macroscopic stress-strain behaviour in which, after the initial elastic loading phase, where is no stress relaxation but rather a slow stress increase akin to the behaviour of a strain hardening creeping material. In this case, the PDFs of the macroscopic damage increment are upper-truncated power laws.

For small values of α and small values of δd (e.g., see figure 9a or 10a for $\alpha = 2$ and $\delta d = 0.1$), the macroscopic behaviour, showing very sharp but small amplitude stress drops at each loading-unloading cycle, is reminiscent of a quasi-brittle material in which the stress relaxation through viscous-like deformation is insignificant. Each stress unloading phase is associated with a large avalanche of damage events that spans the entire domain. This explains the sharp mode in the PDF of the macroscopic damage increments at large increment values, which indicates that a characteristic avalanche size emerges, associated to a finite-size effect.

For large values of α and small values of δd (e.g., see figure 9 or 10, d and e, for $\alpha = 6$ or 8), the dissipation of stresses at the onset of damaging is the largest and the material becomes readily fluid-like. The stress is regularly and completely dissipated at each loading-unloading cycle. Local damage events are suppressed, which is expressed by the translation of the PDF of macroscopic damage increments towards larger increment values. The elastic redistribution of stresses are inhered and, therefore, the spatio-temporal correlations in the damaging activity are limited, which reduces the horizontal extent of avalanches and explains the appearance of broad modes in the PDFs of damage increments as well as their departure from a power law.

For intermediate values of α (e.g., $\alpha = 3, 4$, see figure 9 or 10, b and c) and small values of δd (0.1, 0.3, 0.5), the distribution of damage increments can be well-fitted with a power-law, that extents at large damage increment values. This suggests that the model simulates a mechanical behaviour that is, at least to some extent, scale-invariant. Unloading phases are characterized by stress drops of variable amplitudes, which are initially almost-instantaneous and then followed by a transient period.

6 Discussions

In this section, we further discuss what the model in its current state is able and not able to simulate in the context of fault deformation and slow earthquakes. To do so, we investigate the simulated dynamical behaviour for one specific case in which only δd is varied and all other mechanical parameters are identical. This simulation is identified by the black box on figure 10c and uses $\mathrm{De}_0 = 0.1$, $\alpha = 4$, with the corresponding default values of $\tilde{\Delta t}$ and T_h (see table 3). In particular, we analyze the temporal evolution of pointwise displacements and velocities at the top boundary of the domain, which constitute proxies for the surface displacements and velocities as measured by Global Positioning Systems (GPS). In the following, we focus on the horizontal displacement and velocity at one point, the top left corner of the domain, which is furthest from the top right corner and therefore less influenced by the prescribed boundary condition there ($u_x = 0$). It is important to note that on figures 11a, b and e, f, the prescribed velocity forcing, U, is subtracted from the recorded horizontal surface velocity. Also, the first few loading-unloading cycles are omitted from the analysis, as they are susceptible to carry the signature the first (outlier) rupture event.

The comparison of two simulations in which only the damage increment is varied between 0.1 and 0.5, summarized in figure 11, suggests that over a certain range of mechanical parameters the model can reproduce two different types of mechanical behaviour, which are more analogous to classical earthquakes and slow slip events, respectively. In the first case ($\delta d = 0.1$, left panels), the macroscopic shear stress on the top boundary indeed shows very rapid and large-amplitude release phases followed by short post-seismic stress relaxation phases and much longer reloading phases (see figure 11a). Each brutal stress release event is associated with a sharp reversal of the surface horizontal ($x-$) velocity and an equally sharp drop in the surface horizontal displacement (see figure 11c), which suggests a strong decoupling of the upper and lower plates following large damage events, reminiscent of classical earthquakes. In the second case ($\delta d = 0.5$, right panels), the asymmetry in the loading-unloading cycles is much less pronounced (see figures 11b and d): the stress is much more progressively dissipated at each loading-unloading cycle, which is accompanied by lower amplitude variations of the surface velocity and a progressive decrease in the surface displacement, reminiscent of slow slip events (e.g., Rogers & Dragert, 2003; Radiguet et al., 2016).

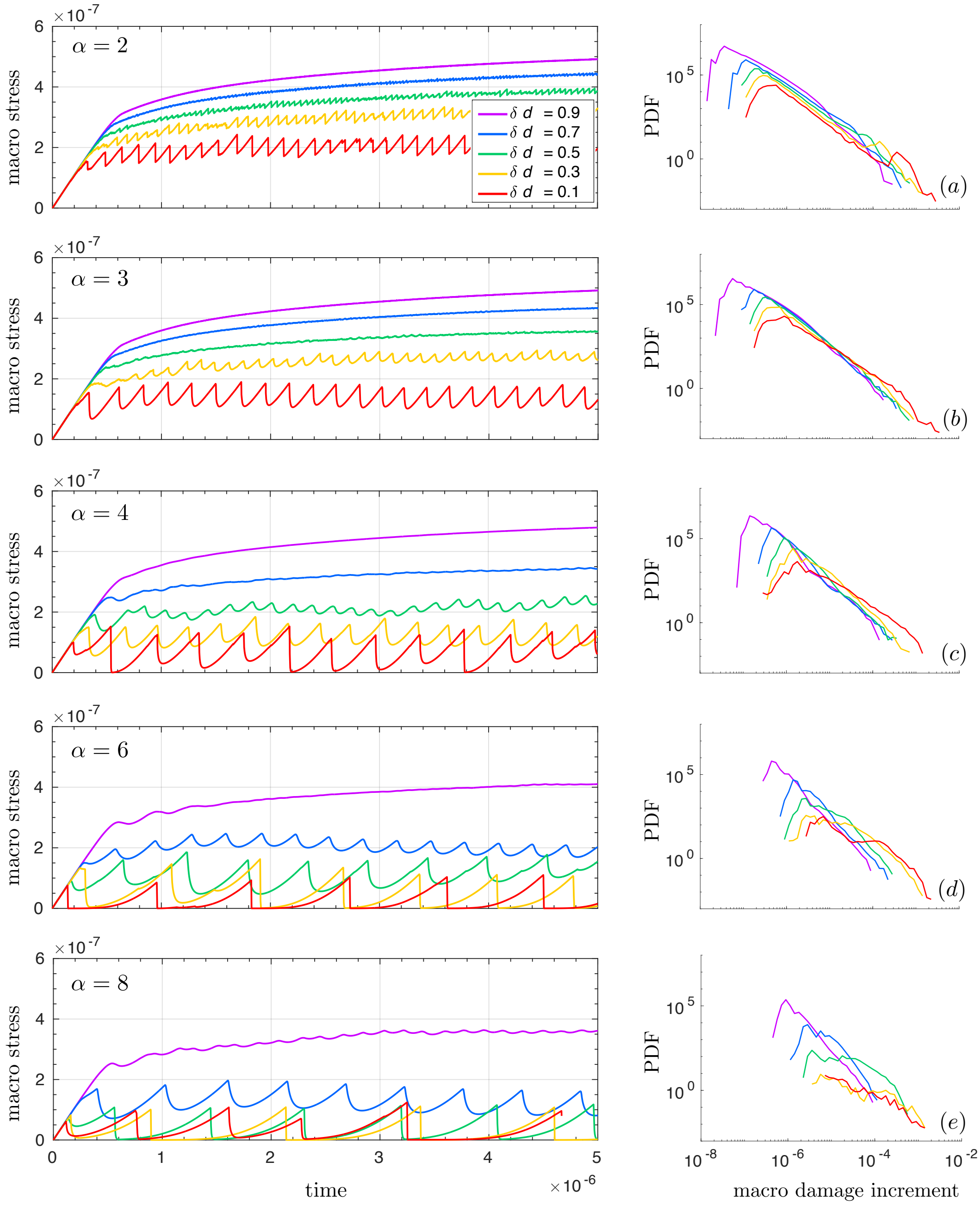

Figure 9. Time series of the macroscopic stress (left panels) and probability density function of the macroscopic damage increment (right panels) for $\mathrm{De}_0 = 0.001$ ($\tilde{\Delta t} = 10^{-10}$, $T_h = 10^{-5}$) and $\delta d = 0.1, 0.3, 0.5, 0.7, 0.9$ and (a) $\alpha = 2$, (b) $\alpha = 3$, (c) $\alpha = 4$, (d) $\alpha = 6$, (e) $\alpha = 8$.

The damaging activity also differs between the two cases (see figures 11c, d). In the first, fewer damage events are recorded over the same simulation time. The damaging activity concentrates over large events that either precede (as in foreshocks) or coincide with stress release phases. In the second case, the damaging activity is more symmetric with respect to unloading phases, with damaging event both preceding (as in foreshocks) and following (as in aftershocks) stress release events.

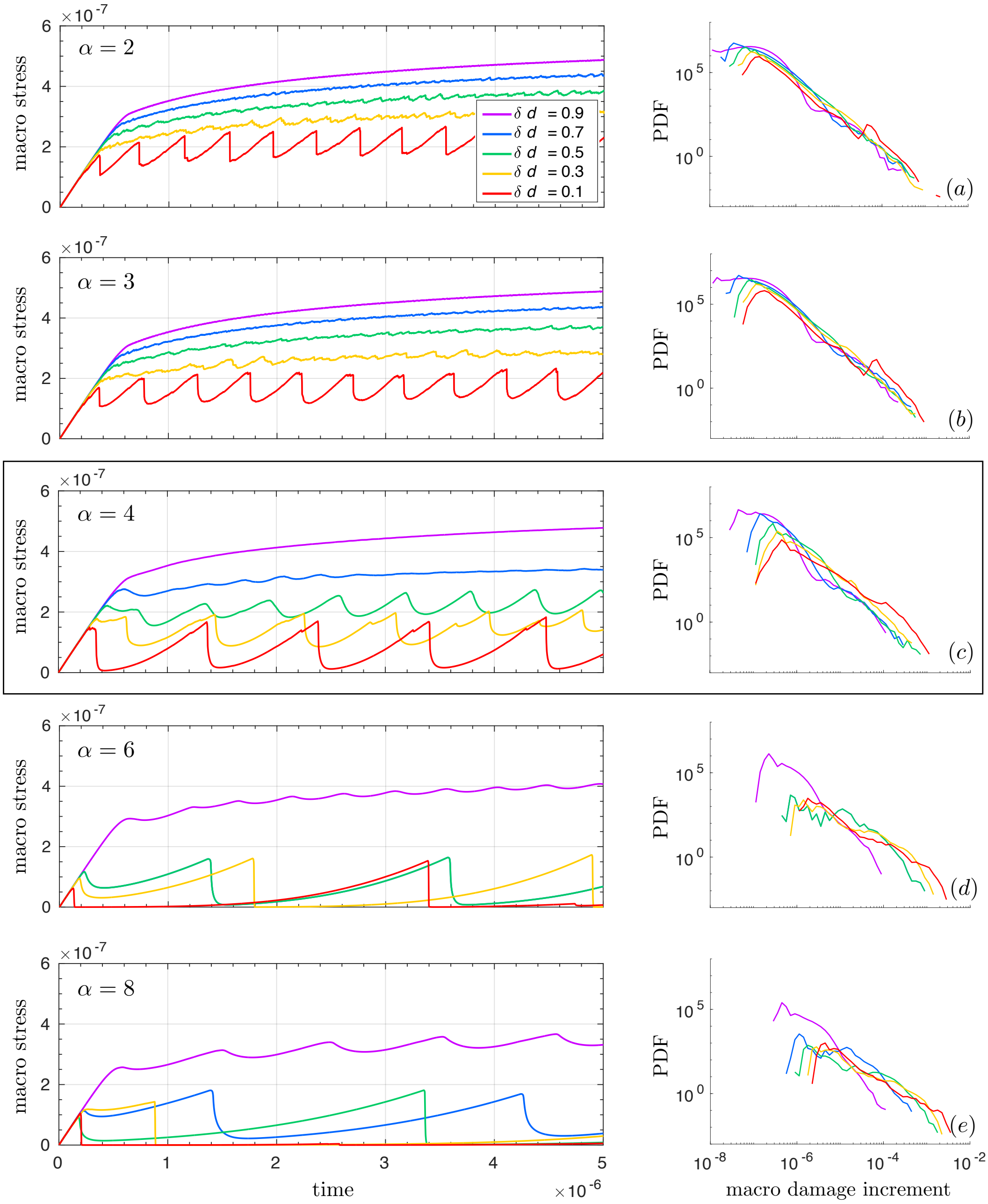

Figure 10. Time series of the macroscopic stress (left panels) and probability density function of the macroscopic damage increment (right panels) for $\mathrm{De}_0 = 0.1$ ($\tilde{\Delta t} = 10^{-10}$, $T_h = 10^{-5}$) and $\delta d = 0.1, 0.3, 0.5, 0.7, 0.9$ and (a) $\alpha = 2$, (b) $\alpha = 3$, (c) $\alpha = 4$, (d) $\alpha = 6$, (e) $\alpha = 8$.

We further analyze the temporal evolution of the surface horizontal velocity during each loading-unloading cycle, that is, over a period of time that starts at the onset of each stress release phase and extents until the next phase, as delimited by the dashed lines and arrows on figures 11a, b and c, d. In the first case, using $\delta d = 0.1$, the model reproduces a power law decay of the velocity of the form

$$V(t) \sim \frac{1}{t^p}, \tag{20}$$

where t is the time after the onset of stress release, and the exponent p is slightly smaller than 1 (see figure 11e). This behaviour is akin to the observed Omori-like decay of post-earthquake surface velocities (Perfettini & Avouac, 2004; Savage et al., 2005; Ingleby & Wright, 2017; Periollat et al., 2022), which suggests that long-term temporal correlations in the system control the evolution of post-earthquake surface velocities in the case of classical earthquakes. It is important to note however that in the present case, this trend spans a little more than two orders of magnitude, which is much less than what the observations cover. This is due to the fact that, for the purpose of this paper, we have chosen our mechanical parameters (in particular the ratio C_0/E_0, which controls the system loading time, see section 5.3.1) to be consistent with the typical recurrence time of slow earthquakes, not with the larger time scales associated with classical earthquakes.

In the second case, using $\delta d = 0.5$, the post-rupture surface velocities are significantly smaller than in the previous case, and remain relatively stable for some time, before slowly decaying at larger timescales (see figure 11f). Such behaviour is similar to what is observed during some largest SSEs for which the details of the displacement time series can be resolved (Cotte et al., 2009; Radiguet et al., 2012).

These results suggest that the proposed modeling framework could be able to reproduce both slow earthquakes and classical earthquakes. Numerically at least, it can do it because it is efficient enough.

One important point however is that, not over the entire range of model parameter values but over the range that generates a mechanical behaviour most analogous to slow and classical earthquakes, the model definitely exhibits a pseudo-periodic behaviour. While it might be consistent with slow earthquakes (e.g., Dragert et al., 2001; Cotte et al., 2009; Radiguet et al., 2016), such behaviour is less consistent with classical earthquakes. While recent studies have found that large (classical) earthquakes occur more regularly than a purely random process (e.g., T. Williams et al., 2019; Griffin et al., 2020), the temporal evolution of classical earthquakes in general is indeed more intermittent and their recurrence time, hardly predictable (e.g., Gardner & Knopoff, 1974; Michael, 2011). We however believe that more variability in recurrence times and stress drop magnitudes and an intermittent behaviour covering a wider range of time scales could be obtained by incorporating additional physical components to the model. Leaving aside the more complex dynamics of fluids aspects, we list some simple and logical options below.

The first consists in moving to a healing law that does not prescribe a unique, constant healing time. Such a law would be in better agreement with available observations. Measurements of relative seismic velocity changes after majors earthquakes indeed indicate a healing rate that is not constant but decrease in time after the main shock, suggesting that the damaged region within the fault regains strength rapidly in the early stage of the interseismic period and progressively more slowly in the later stages (e.g., Li & Vidale, 2001; Brenguier et al., 2008). In the present model, this behaviour could be parameterized through a logarithmic healing law that does not include any characteristic time for healing but that instead depends locally on the time elapsed since the last damage event. Such a law would agree with the aging version of the rate-and-state interface model of (Ruina, 1983), which imply that the surfaces that are in contact and at rest strengthen logarithmically and would allow the system to evolve in a less deterministic manner.

The second consists in accounting for a representation of the rheological stratification of subduction zones, which is known to depend strongly on temperature (e.g. Peacock, 2009) and therefore on depth. In the present 2-dimensional, idealized numerical experiments, this stratification could be coarsely accounted for by allowing the bulk, undamaged viscosity of the host rock in the two plates to vary as a simple function (for instance, linear) of the horizontal distance (x) parallel to the interface, so that to repre-

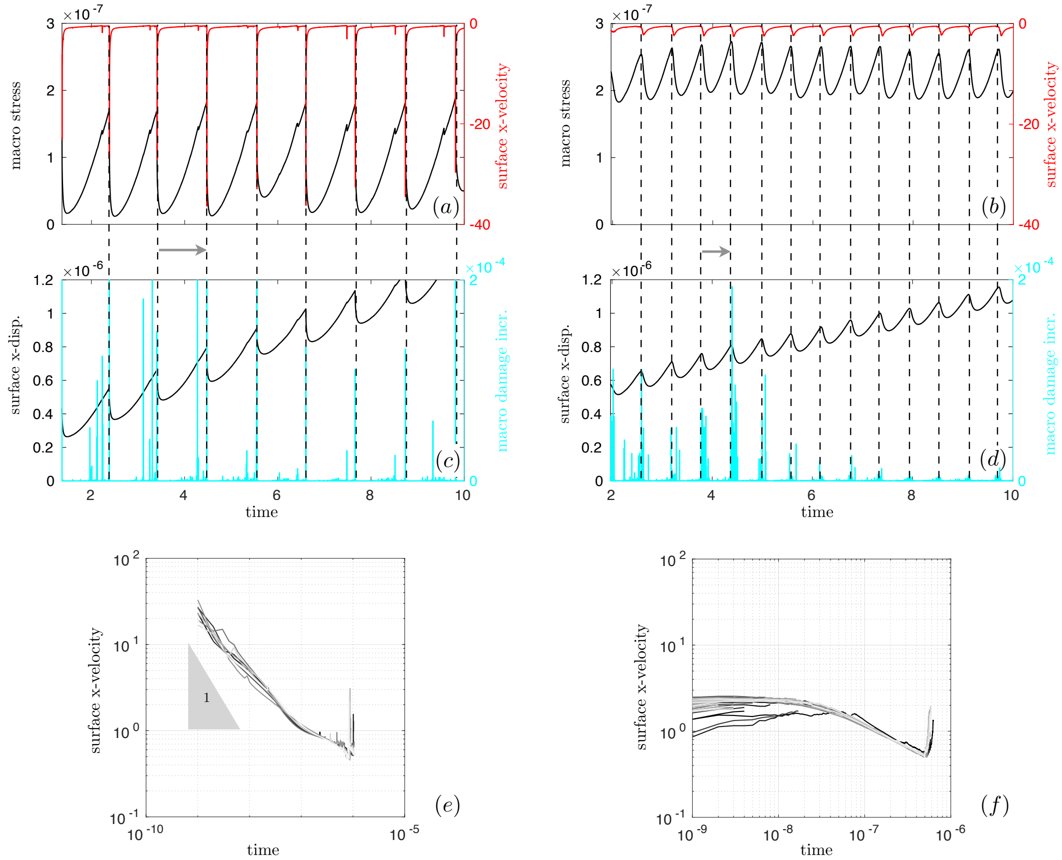

Figure 11. (a, b) Temporal evolution of the macroscopic stress (black curve) and of the surface x-velocity at the upper left corner of the domain (red curve) for a simulation in which $\mathrm{De}_0 = 0.1$ ($\tilde{\Delta t} = 10^{-9}$, $T_h = 10^{-4}$), $\alpha = 4$ and (a) $\delta d = 0.1$ and (b) $\delta d = 0.5$. (c, d) Corresponding temporal evolution of the cumulated surface x-displacement at the upper left corner of the domain (black curve) and of macroscopic damage increment (cyan curve). (e, f) Corresponding surface x-velocity at the upper left corner of the domain as a function of the time elapsed between each unloading event, as indicated by the dashed lines and arrows on figures (a) to (d). In figures a, b, e and f, the prescribed forcing velocity, U, is subtracted from the $x-$velocity.

sent a more brittle (high viscosity) behaviour towards the surface and a more ductile (low viscosity) behaviour at depth. Such a dependence of the viscosity with depth would allow mitigating the impact of finite size effects and at the same time, exploring spatial and temporal interactions between the different types of mechanical behaviours simulated by the model, that is, an essentially brittle behaviour akin to low-depth, classical earthquakes, a mixed brittle-ductile behaviour akin to slow-slip events and diffuse, ductile deformations akin to the deeper parts of subduction zones. In the same line of ideas, the use of the full Burger model, that is, incorporating the Kelvin component that was left aside in the present experiments but which is meant to accounts for the deformation of the mantle (e.g., Nur & Mavko, 1974; Pollitz et al., 2001), would act as an additional source of post-seismic transient deformation and as such would bring some extra complexity in the temporal behaviour of the model.

The third addition would account for friction, which most likely plays a first-order role in the brittle part of the shear zone (e.g., Byerlee, 1967; Scholz, 1998, and many others), where asperities can become locked, thereby allowing for stresses to locally build-up and local quakes to be triggered. To simulate the effect of static friction in a simple manner, an additional threshold on the the minimum stress required for the occurrence of viscous deformation (as opposed to damage) could be coupled to the viscous stress dissipation term of equation 1. This criterion, of the cohesion-less Mohr-Coulomb type, would ensure that for low states of stress, slip would be hindered and elastic stresses would build-up locally towards critically.

7 Conclusions

In this paper, we have presented a continuum, volumetric mechanical model suited for modelling slow earthquakes. We have also presented a numerical framework for this model that is efficient enough to cover several deformation cycles in very reasonable simulation times in a 2-dimensional setup, while allowing to resolve both the very short-term and localized damage initiation and propagation processes associated with the co-seismic rupture and the diffuse deformations within the bulk of the host rock that relaxes stresses over very long time scales. In between these very short and very long time scales and over a certain range of parameters, the model can simulate a correlated seismic (i.e., damage) activity as well as different transient, seismic and aseismic processes akin to classical and slow earthquakes, such as the post-seismic stress relaxation phase.

In particular, the fact that the model can reproduce the observed Omori-like decay in surface post-seismic velocities over a certain range of mechanical parameter values, even in the presently highly idealized simulation setup, is an important result, as it supports the hypothesis of (Ingleby & Wright, 2017) that visco-elastic models, either of the Maxwell or the Burgers type, require a continuously varying viscosity or, equivalently, a continuously varying relaxation time, to reproduce this observed trend. Here, this continuous variation in the relaxation time is achieved by applying a unique rheological law over the entire system, hence avoiding the need to prescribe the mechanical behaviour in different parts of the system or the location of the shearing zone, but letting both the elastic modulus and viscosity evolve in time and in space as simple functions of the level of damage.

Leaving aside for the moment the inclusion of the dynamics of fluids, we have suggested several simple additions to the current rheological framework that aim at extending its application to the representation of the entire seismic "cycle": that is a deformation that comprises both classical and slow earthquakes. The one-by-one inclusion of these additions - a logarithmic, time-since-damage-dependant healing law, a variation of the viscosity with depth and a deformation threshold for static friction -, the evaluation of their respective impact on the simulated mechanical behaviour and the assessment of their relative contribution towards a more realistic reproduction of the deformation cycle of faults is the aim of our next paper.

Appendix A Adimensional system of equations

The model is made adimensional with respect to

1. the horizontal extent, L, of the domain in the direction of the forcing,
2. the prescribed forcing velocity, U,
3. the undamaged elastic modulus, E_0.

The time characterizing the deformation process is therefore $T = \frac{L}{U}$. In the following, the superscript '$\tilde{}$' is used for all dimension-less variables and operators, which are listed in table A1.

Variables, dimensions and operators		Non-dimensional equivalent
Spatial (2D) dimension	$\mathbf{x}$	$\tilde{\mathbf{x}} = \frac{\mathbf{x}}{L}$
Time	t	$\tilde{t} = \frac{t}{T}$
Velocity	$\mathbf{u}$	$\tilde{\mathbf{u}} = \frac{\mathbf{u}}{U}$
Internal stress	σ	$\tilde{\sigma} = \frac{\sigma}{E_0}$
Level of damage	d, d'	d, d'
Del Operator	∇	$\tilde{\nabla} = L\nabla$

Table A1. Dimensional model variables and operators and their adimensional counterpart.

In terms of these adimensional variables and operators, the momentum equation reads:

$$\tilde{\nabla} \cdot \tilde{\sigma} = 0 \tag{A1}$$

for either the pre- or post-damage stress, σ or σ'.

The full constitutive equation becomes

$$\frac{U}{L} E_0 \frac{\partial \tilde{\sigma}}{\partial \tilde{t}} + \frac{E_0}{\lambda_0 (1 - d^{\alpha-1})} \tilde{\sigma} = \frac{U}{L} E_0 (1-d) \mathbf{K} \colon \tilde{\dot{\varepsilon}},$$

or

$$\frac{\partial \tilde{\sigma}}{\partial \tilde{t}} + \frac{1}{\mathrm{De}_0 (1-d)^{\alpha-1}} \tilde{\sigma} = (1-d) \mathbf{K} \colon \tilde{\dot{\varepsilon}}, \tag{A2}$$

where $\mathrm{De}_0 = \frac{\eta_0}{E_0} \frac{U}{L}$ is the (undamaged) Deborah number. The constitutive equation for the post-damage stress redistribution is:

$$\tilde{\sigma'} - \delta d \tilde{\sigma} = (1-d') \mathbf{K} \colon \tilde{\varepsilon}. \tag{A3}$$

Damage being a non-dimensional variable, the damage equation (5) is itself adimensional:

$$1 - d' = \delta d \left(1 - d\right). \tag{A4}$$

The adimensional healing equation reads

$$\frac{1}{T} \frac{\partial d'}{\partial \tilde{t}} = -\frac{1}{t_h} d', \; 0 \le d' < 1,$$

or

$$\frac{\partial d'}{\partial \tilde{t}} = -\frac{1}{T_h} d', \; 0 \le d' < 1. \tag{A5}$$

where $T_h = \frac{t_h}{T}$.

Appendix B Numerical Scheme

Here we present the time discretization and the numerical algorithm employed to solve the system of equations in the shearing experiments. For simplicity, the superscript $'\tilde{}'$ for adimensional variables is drop in the following notations.

This system of equations (A1 for σ and for σ', A2, A3, A4, A5) forms a problem that is solved for the following unknowns : $\dot{\varepsilon}$ and ε' (3 components each), σ and σ' (3 components each) and d', starting from an initial state of rest and zero damage. It is solved over a closed 2-dimensional domain $\Omega \in \mathbb{R}$ (see figure 4), with an external boundary partitioned as $\partial\Omega = \Gamma_{\text{top}}, \Gamma_{\text{bottom}}, \Gamma_{\text{left}}, \Gamma_{\text{right}}$. A constant $x-$velocity is applied on Γ_{bottom}. It is fixed to 0 during the steady-state, stress redistribution process. The $z-$velocity is fixed to 0 on Γ_{bottom} and $u_x = 0$ on the right upper corner of the domain. The top and lateral boundaries are free, hence $\sigma \cdot \mathbf{n} = 0$ on Γ_{top}, Γ_{left} and Γ_{right}.

B01 Time discretization

We discretize the time, t, such that $t_n = n\Delta t$, with $\Delta t > 0$ and $n = 0, 1, 2, ...$ and use a backward Euler (implicit) scheme of order 1. Expressing the strain rate tensor as $\dot{\varepsilon} = D(\mathbf{u}) = \frac{1}{2}\left(\nabla\mathbf{u} + \nabla\mathbf{u}^T\right)$ and the strain tensor as $D(\mathbf{u})\Delta t$, the time-discretized system of equations reads:

$$
\begin{aligned}
\nabla \cdot \sigma^{n+1} &= 0, \\
\frac{\sigma^{n+1} - \sigma^n}{\Delta t} + \frac{1}{\text{De}_0\,(1-d^n)^{\alpha-1}}\sigma^{n+1} &= (1-d^n)\,\mathbf{K}\colon D(\mathbf{u}^{n+1}), \\
1 - d'^n &= \delta d\,(1-d^n) \\
\nabla \cdot \sigma'^{n+1} &= 0, \\
\sigma'^{n+1} - \delta d \sigma^{n+1} &= (1-d'^n)\mathbf{K}\colon D(\mathbf{u}'^{n+1}\Delta t), \\
\frac{d'^{n+1} - d'^n}{\Delta t} &= -\frac{1}{T_h} d'^n,\ 0 < d'^{n+1} \leq 1.
\end{aligned}
$$

The numerical scheme divides this time-discretized problem, P_d, into three subproblems. Using the superscript $k = 0, 1, 2, ...$ for the steady-state stress-redistribution subiteration in subproblem 2, these problems reads:

- ($P1_d$) The momentum and constitutive equations are first solved simultaneously for the fields of velocity and stress, σ^{n+1} and $\mathbf{u}^{n+1}$ at the current time step, by applying the constant $x-$velocity forcing on Γ_{bottom} and the other boundary conditions and using the level of damage at the previous time step, d^n.
- ($P2_d$) The steady-state stress redistribution equations are solved iteratively, with the $x-$velocity on Γ_{bottom} now set to zero. In this subproblem, the damage equation is first solved for $d'^{n,k+1}$ by comparing the field of stress at the current subiteration, $\sigma^{n+1,k}$, to the local damage criteria, σ_c. The updated level of damage is then substituted into the post-damage constitutive equation. Together with the momentum equation, it is solved for the adjusted fields of velocity, $\mathbf{u}'^{n+1,k+1}$, and stress, $\sigma'^{n+1,k+1}$. These steps are iterated until all of the adjusted stresses become sub-critical. Then the post-damage level of damage, d'^n, is set to $d'^{n,k+1}$.
- ($P3_d$) The healing equation is finally solved for the level of damage at the current time step, d'^{n+1} and d^{n+1} is set to d'^{n+1}.

The complete algorithm reads:

Initialization ($n = 0$)

$$
\begin{aligned}
\mathbf{u}^n &= 0 \text{ in } \Omega, \\
\sigma^n &= 0 \text{ in } \Omega, \\
d^n = d'^n &= 0 \text{ in } \Omega.
\end{aligned}
$$

For $n \geq 0$, set $k = 0$

$(P1_d)$ *With σ^n and d^n known, find σ^{n+1} and $\mathbf{u}^{n+1}$ such that*

$$\begin{aligned}\nabla\cdot\sigma^{n+1} &= 0,\\ \frac{\sigma^{n+1}-\sigma^n}{\Delta t}+\frac{1}{\mathrm{De}_0\,(1-d^n)^{\alpha-1}}\sigma^{n+1} &= (1-d^n)\,\mathbf{K}\colon D(\mathbf{u}^{n+1}),\end{aligned}$$

and with

$$\begin{aligned}u_z^{n+1} &= 0 \text{ on } \Gamma_{\text{bottom}},\\ u_x^{n+1} &= 1 \text{ on } \Gamma_{\text{bottom}},\\ u_x^{n+1} &= 0 \text{ on } \Gamma_{\text{top}}\cap\Gamma_{\text{right}},\\ \sigma^{n+1}\cdot\mathbf{n} &= 0 \text{ on } \Gamma_{\text{top}},\Gamma_{\text{left}} \text{ and } \Gamma_{\text{right}},.\end{aligned}$$

IF anywhere in Ω $\sigma_1^{n+1} > q\sigma_2^{n+1}+\sigma_c$, set $\sigma'^{n+1,k}=\sigma^{n+1}$ and $d'^{n,k}=d^n$.

$(P2_d)$ For $k\geq 0$,

1. *Find $d'^{n,k+1}$ such that*
$$1-d'^{n,k+1}=\delta d\left(1-d'^{n,k}\right),$$
2. *Find $\sigma^{n+1,k+1}$ and $\mathbf{u}^{n+1,k+1}$ such that*

$$\begin{aligned}\nabla\cdot\sigma^{n+1,k+1} &= 0,\\ \sigma'^{n+1,k+1}-\delta d\sigma'^{n+1,k} &= E_0(1-d'^{n,k+1})\mathbf{K}\colon\left(D(\mathbf{u}'^{n+1,k+1})\Delta t\right)\end{aligned}$$

and with

$$\begin{aligned}u_z'^{n+1,k+1} &= 0 \text{ on } \Gamma_{\text{bottom}},\\ u_x'^{n+1,k+1} &= 0 \text{ on } \Gamma_{\text{bottom}},\\ u_x'^{n+1,k+1} &= 0 \text{ on } \Gamma_{\text{top}}\cap\Gamma_{\text{right}},\\ \sigma'^{n+1,k+1}\cdot\mathbf{n} &= 0 \text{ on } \Gamma_{\text{top}},\Gamma_{\text{left}} \text{ and } \Gamma_{\text{right}},.\end{aligned}$$

IF $\sigma_1'^{n+1,k+1}\leq q\sigma_2'^{n+1,k+1}+\sigma_c$,
STOP and set $\sigma^{n+1}=\sigma'^{n+1,k+1}$ and $d'^n=d'^{n,k+1}$ $(P3_d)$ Find d'^{n+1} such that

$$\frac{d'^{n+1}-d'^n}{\Delta t}=-\frac{1}{T_h}d'^n,\ 0<d'^{n+1}\leq 1.$$

Set $d^{n+1}=d'^{n+1}$.

Appendix C Convergence

Figure C1 shows the probability density function of $E_{brit}/\tilde{\Delta t}$ obtained in the case of $\mathrm{De}_0=0.1$ and $\mathrm{De}_0=10$, using $\alpha=4$, $\delta d=0.1$ and $T_h=10^{-4}$ and $T_h=10^{-3}$ respectively. The PDFs indicate that the macroscopic model response converges as $\tilde{\Delta t}$ is decreased, as for the case of $\mathrm{De}_0=0.001$ described in section 5.2. The values of $\tilde{\Delta t}$ for which the response is not converged are indicated in red in table 3. The value of $\tilde{\Delta t}$ corresponding to each De_0 value and used in the sensitivity analyses on T_h, α and δd are indicated in green in the same table.

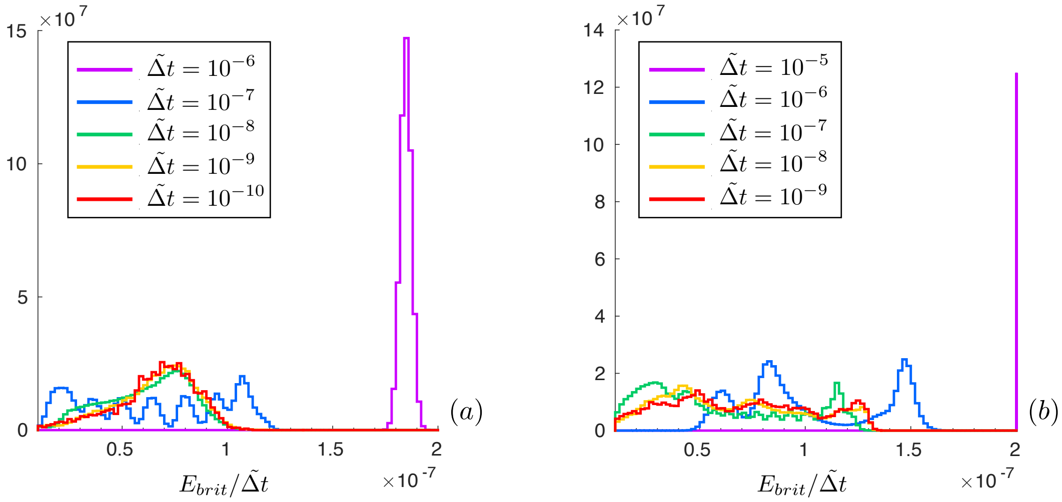

Figure C1. Probability density function of $E_{brit}/\tilde{\Delta t}$ for simulations using $\alpha = 4$, $\delta d = 0.1$ and (a) $\text{De}_0 = 0.1$, $T_h = 10^{-4}$ and $\tilde{\Delta t} = 10^{-10}, 10^{-9}, 10^{-8}, 10^{-7}, 10^{-6}$ and (b) $\text{De}_0 = 10$, $T_h = 10^{-3}$ and $\tilde{\Delta t} = 10^{-9}, 10^{-8}, 10^{-7}, 10^{-6}, 10^{-5}$ (corresponding to $\Delta t = 10^4$ s, 10^5 s, 10^6 s, 10^7 s, 10^8 s respectively).

Acknowledgments

The authors thank David Amitrano and Jean-Luc Got for insightful discussions about this paper and related topics. V. D., N. S. and M. C. acknowledge support from the European Research Council (ERC) under the European Union's Horizon 2020 research and innovation program (Grant agreements no 787399, SEISMAZE for N. S. and V. D. and 742335, F-IMAGE for M. C.).

The outputs of numerical simulations can be found at: XXXZenodo. The post-processing MATLAB codes used to produce the figures and movie presented in this paper and SI are available at: `https://github.com/vdansereau/Multi-Scale-Deformation-Cycle-AGU-Solid-Earth-paper.git`. The model equations and the numerical scheme (time and space discretizations) are fully described in sections 2.4 and 3 of the main text and in the Appendix A and Appendix B, to allow reproducibility. The C++ library RHEOLEF used to set the domain and boundary conditions and to solve the set of equations is documented and available for download at `https://membres-ljk.imag.fr/Pierre.Saramito/rheolef/html/index.html`.

References

Amitrano, D. (2003). Brittle-ductile transition and associated seismicity: Experimental and numerical studies and relationship with the b value. *Journal of Geophysical Research*, *108*(B1). doi: 10.1029/2001JB000680

Amitrano, D., Grasso, J.-R., & Hantz, D. (1999). From diffuse to localised damage through elastic interaction. *Geophysical Research Letters*, *26*(14), 2109-2112.

Angiboust, S., Kirsch, J., Oncken, O., G., J., Monié, P., & Rybacki, E. (2015). Probing the transition between seismically coupled and decoupled segments along an ancient subduction interface. *Geochemistry, Geophysics, Geosystems*, *16*(6), 1905-1922. Retrieved from `https://agupubs.onlinelibrary.wiley.com/doi/abs/10.1002/2015GC005776` doi: https://doi.org/10.1002/2015GC005776

Ashby, M. F., & Sammis, C. G. (1990). The damage mechanics of brittle solids in compression. *pure and applied geophysics*, *133*(3), 489–521. Retrieved from https://doi.org/10.1007/BF00878002 doi: 10.1007/BF00878002

Audet, P., Bostock, M., Christensen, N., & Peacock, S. M. (2009). Seismic evidence for overpressured subducted oceanic crust and megathrust fault sealing. *Nature*, *457*(7225), 76–78. doi: 10.1038/nature07650

Ben-Zion, Y., & Lyakhovsky, V. (2002). Accelerated seismic release and related aspects of seismicity patterns on earthquake faults. In M. Matsu'ura, P. Mora, A. Donnellan, & X.-c. Yin (Eds.), *Earthquake processes: Physical modelling, numerical simulation and data analysis part ii* (pp. 2385–2412). Basel: Birkhäuser Basel. Retrieved from https://doi.org/10.1007/978-3-0348-8197-5_12 doi: 10.1007/978-3-0348-8197-5_12

Ben-Zion, Y., & Lyakhovsky, V. (2006, 04). Analysis of aftershocks in a lithospheric model with seismogenic zone governed by damage rheology. *Geophysical Journal International*, *165*(1), 197-210. Retrieved from https://doi.org/10.1111/j.1365-246X.2006.02878.x doi: 10.1111/j.1365-246X.2006.02878.x

Bhat, H. S., Rosakis, A. J., & Sammis, C. G. (2012, 04). A Micromechanics Based Constitutive Model for Brittle Failure at High Strain Rates. *Journal of Applied Mechanics*, *79*(3). Retrieved from https://doi.org/10.1115/1.4005897 (031016) doi: 10.1115/1.4005897

Bos, B., & Spiers, C. J. (2002). Fluid-assisted healing processes in gouge-bearing faults: Insights from experiments on a rock analogue system. *pure and applied geophysics*, *159*(11), 2537–2566. Retrieved from https://doi.org/10.1007/s00024-002-8747-2 doi: 10.1007/s00024-002-8747-2

Bostock, M. G., Royer, A. A., Hearn, E. H., & Peacock, S. M. (2012). Low frequency earthquakes below southern vancouver island. *Geochemistry, Geophysics, Geosystems*, *13*(11), Q11007. doi: https://doi.org/10.1029/2012GC004391

Brenguier, F., Campillo, M., Hadziioannou, C., Shapiro, N. M., Nadeau, R. M., & Larose, E. (2008). Postseismic relaxation along the san andreas fault at parkfield from continuous seismological observations. *Science*, *321*(5895), 1478–1481. Retrieved from https://science.sciencemag.org/content/321/5895/1478 doi: 10.1126/science.1160943

Brown, K. M., Tryon, M. D., DeShon, H. R., Dorman, L. M., & Schwartz, S. Y. (2005). Correlated transient fluid pulsing and seismic tremor in the costa rica subduction zone. *Earth and Planetary Science Letters*, *238*(1), 189-203. doi: https://doi.org/10.1016/j.epsl.2005.06.055

Brudzinski, M. R., & Allen, R. M. (2007, 10). Segmentation in episodic tremor and slip all along Cascadia. *Geology*, *35*(10), 907-910. doi: 10.1130/G23740A.1

Burov, E. B. (2011). Rheology and strength of the lithosphere. *Marine and Petroleum Geology*, *28*(8), 1402 - 1443. Retrieved from http://www.sciencedirect.com/science/article/pii/S0264817211001425 doi: https://doi.org/10.1016/j.marpetgeo.2011.05.008

Burridge, R., & Knopoff, L. (1967). Model and theoretical seismicity. *Bulletin of the Seismological Society of America*, *57*(3), 341-371.

Byerlee, J. D. (1967). Frictional characteristics of granite under high confining pressure. *Journal of Geophysical Research*, *72*(14), 3639–3648. Retrieved from http://dx.doi.org/10.1029/JZ072i014p03639 doi: 10.1029/JZ072i014p03639

Byerlee, J. D. (1978). Friction of rocks. *Pure and Applied Geophysics*, *116*, 615–626. doi: https://doi.org/10.1007/BF00876528

Caine, J. S., Evans, J. P., & Forster, C. B. (1996, 11). Fault zone architecture and permeability structure. *Geology*, *24*(11), 1025-1028. Retrieved from https://doi.org/10.1130/0091-7613(1996)024<1025:FZAAPS>2.3.CO;2 doi: 10.1130/0091-7613(1996)024⟨1025:FZAAPS⟩2.3.CO;2

Carlson, J. M., & Langer, J. S. (1989). Properties of earthquakes generated by fault dynamics. *Phys. Rev. Lett.*, *62*, 2632–2635. Retrieved from https://link.aps.org/doi/10.1103/PhysRevLett.62.2632 doi: 10.1103/PhysRevLett.62.2632

Carrier, A., Got, J.-L., Peltier, A., Ferrazzini, V., Staudacher, T., Kowalski, P., & Boissier, P. (2015, January). A damage model for volcanic edifices: Implications for edifice strength, magma pressure, and eruptive processes. *Journal of Geophysical Research (Solid Earth)*, *120*(1), 567-583. doi: 10.1002/2014JB011485

Chen, J., Niemeijer, A. R., & Spiers, C. J. (2017). Microphysically derived expressions for rate-and-state friction parameters, a, b, and dc. *Journal of Geophysical Research: Solid Earth*, *122*(12), 9627-9657. Retrieved from https://agupubs.onlinelibrary.wiley.com/doi/abs/10.1002/2017JB014226 doi: https://doi.org/10.1002/2017JB014226

Cotte, N., Walpersdorf, A., Kostoglodov, V., Vergnolle, M., Santiago, J.-A., & Campillo, M. (2009). Anticipating the next large silent earthquake in mexico. *Eos, Transactions American Geophysical Union*, *90*(21), 181-182. doi: https://doi.org/10.1029/2009EO210002

Cruz-Atienza, V. M., Villafuerte, C., & Bhat, H. S. (2018). Rapid tremor migration and pore-pressure waves in subduction zones. *Nature Communications*, *9*(1), 2900. doi: 10.1038/s41467-018-05150-3

Dansereau, V. (2016b). *A Maxwell-Elasto-Brittle model for the drift and deformation of sea ice* (Theses, Université Grenoble Alpes). Retrieved from https://tel.archives-ouvertes.fr/tel-01316987

Dansereau, V., Weiss, J., Saramito, P., & Lattes, P. (2016a). A Maxwell-elasto-brittle rheology for sea ice modelling. *The Cryosphere*, *10*, 1339–1359.

Dieterich, J. H. (1978). Time-dependent friction and the mechanics of stick-slip. *pure and applied geophysics*, *116*(4), 790–806. Retrieved from https://doi.org/10.1007/BF00876539 doi: 10.1007/BF00876539

Dieterich, J. H. (1979a). Modeling of rock friction: 1. experimental results and constitutive equations. *Journal of Geophysical Research: Solid Earth*, *84*(B5), 2161-2168. Retrieved from https://agupubs.onlinelibrary.wiley.com/doi/abs/10.1029/JB084iB05p02161 doi: https://doi.org/10.1029/JB084iB05p02161

Dieterich, J. H. (1979b). Modeling of rock friction: 2. simulation of preseismic slip. *Journal of Geophysical Research: Solid Earth*, *84*(B5), 2169-2175. Retrieved from https://agupubs.onlinelibrary.wiley.com/doi/abs/10.1029/JB084iB05p02169 doi: https://doi.org/10.1029/JB084iB05p02169

Dragert, H., Wang, K., & James, T. (2001). A silent slip event on the deeper cascadia subduction interface. *Science*, *292*, 1525–1528.

Dragert, H., Wang, K., & Rogers, G. (2004). Geodetic and seismic signatures of episodic tremor and slip in the northern Cascadia subduction zone. *Earth, Planets and Space*, *56*, 1143–1150.

Dublanchet, P. (2019). Fluid driven shear cracks on a strengthening rate-and-state frictional fault. *Journal of the Mechanics and Physics of Solids*, *132*, 103672. doi: https://doi.org/10.1016/j.jmps.2019.07.015

Dziewonski, A. M., & Anderson, D. L. (1981). Preliminary reference earth model. *Physics of the Earth and Planetary Interiors*, *25*(4), 297 - 356. Retrieved from http://www.sciencedirect.com/science/article/pii/0031920181900467 doi: https://doi.org/10.1016/0031-9201(81)90046-7

Farge, G., Jaupart, C., & Shapiro, N. M. (2021). Episodicity and migration of low frequency earthquakes modeled with fast fluid pressure transients in the permeable subduction interface. *Journal of Geophysical Research: Solid Earth*, *126*(9), e2021JB021894. doi: https://doi.org/10.1029/2021JB021894

Frank, W. B., Radiguet, M., Rousset, B., Shapiro, N. M., Husker, A. L., Kostoglodov, V., … Campillo, M. (2015). Uncovering the geodetic signature of silent slip through repeating earthquakes. *Geophysical Research Letters*, *42*, 2774–2779. doi: 10.1002/2015GL063685

Frank, W. B., Shapiro, N. M., Husker, A., Kostoglodov, V., Bhat, H. S., & Campillo, M. (2015). Along-fault pore-pressure evolution during a slow-slip event in guerrero, mexico. *Earth and Planetary Science Letters*, *413*, 135-143. doi: https://doi.org/10.1016/j.epsl.2014.12.051

Frank, W. B., Shapiro, N. M., Husker, A. L., Kostoglodov, V., Gusev, A. A., & Campillo, M. (2016). The evolving interaction of low-frequency earthquakes during transient slip. *Science Advances*, *2*(4). Retrieved from `https://advances.sciencemag.org/content/2/4/e1501616` doi: 10.1126/sciadv.1501616

Frank, W. B., Shapiro, N. M., Husker, A. L., Kostoglodov, V., Romanenko, A., & Campillo, M. (2014). Using systematically characterized low-frequency earthquakes as a fault probe in guerrero, mexico. *Journal of Geophysical Research: Solid Earth*, *119*(10), 7686-7700. Retrieved from `https://agupubs.onlinelibrary.wiley.com/doi/abs/10.1002/2014JB011457` doi: https://doi.org/10.1002/2014JB011457

Frederiksen, S., & Braun, J. (2001). Numerical modelling of strain localisation during extension of the continental lithosphere. *Earth and Planetary Science Letters*, *188*, 241-251.

Gao, X., & Wang, K. (2017). Rheological separation of the megathrust seismogenic zone and episodic tremor and slip. *Nature*, *543*, 416–419. doi: https://doi.org/10.1038/nature21389

Gardner, J. K., & Knopoff, L. (1974, 10). Is the sequence of earthquakes in Southern California, with aftershocks removed, Poissonian? *Bulletin of the Seismological Society of America*, *64*(5), 1363-1367. Retrieved from `https://doi.org/10.1785/BSSA0640051363` doi: 10.1785/BSSA0640051363

Geuzaine, C., & Remacle, J.-F. (2009). Gmsh: A 3-d finite element mesh generator with built-in pre- and post-processing facilities. *International Journal for Numerical Methods in Engineering*, *79*(11), 1309-1331. Retrieved from `https://onlinelibrary.wiley.com/doi/abs/10.1002/nme.2579` doi: https://doi.org/10.1002/nme.2579

Got, J.-L., Carrier, A., Marsan, D., Jouanne, F., Vogfjörd, K., & Villement, T. (2017). An analysis of the non-linear magma-edifice coupling at grimsvötn volcano (iceland). *Journal of Geophysical Research Solid Earth*, *122*. doi: 10.1002/2016JB012905

Griffin, J. D., Stirling, M. W., & Wang, T. (2020). Periodicity and clustering in the long-term earthquake record. *Geophysical Research Letters*, *47*(22), e2020GL089272. Retrieved from `https://agupubs.onlinelibrary.wiley.com/doi/abs/10.1029/2020GL089272` (e2020GL089272 2020GL089272) doi: https://doi.org/10.1029/2020GL089272

Gutemberg, B., & Richter, C. F. (1949). *Seismicity of the earth and associated phenomena.* Princeton NJ USA: Princeton University Press.

Hamiel, Y., Liu, Y., Lyakhovsky, V., Ben-Zion, Y., & Lockner, D. (2004). A viscoelastic damage model with applications to stable and unstable fracturing. *Geophysical Journal International*, *159*, 1155-1165. doi: 10.1111/j.1365-246X.2004.02452.x

Handwerger, A. L., Rempel, A. W., Skarbek, R. M., Roering, J. J., & Hilley, G. E. (2016). Rate-weakening friction characterizes both slow sliding and catastrophic failure of landslides. *Proceedings of the National Academy of Sciences*, *113*(37), 10281–10286. Retrieved from `https://www.pnas.org/content/113/37/10281` doi: 10.1073/pnas.1607009113

Hayman, N. W., & Lavier, L. L. (2014). The geologic record of deep episodic tremor and slip. *Geology*, *42*(3), 195-198. Retrieved from `https://doi.org/10.1130/G34990.1` doi: 10.1130/G34990.1

Hetland, E. A., & Hager, B. H. (2005). Postseismic and interseismic displacements near a strike-slip fault: A two-dimensional theory for general linear viscoelastic rheologies. *Journal of Geophysical Research: Solid Earth*, *110*(B10). Retrieved from https://agupubs.onlinelibrary.wiley.com/doi/abs/10.1029/2005JB003689 doi: https://doi.org/10.1029/2005JB003689

Hetland, E. A., & Hager, B. H. (2006, 07). The effects of rheological layering on post-seismic deformation. *Geophysical Journal International*, *166*(1), 277-292. Retrieved from https://doi.org/10.1111/j.1365-246X.2006.02974.x doi: 10.1111/j.1365-246X.2006.02974.x

Hirono, T., Kaneki, S., Ishikawa, T., Kameda, J., Tonoike, N., Ito, A., & Miyazaki, Y. (2020). Generation of sintered fault rock and its implications for earthquake energetics and fault healing. *Communications Earth & Environment*, *1*(1), 3. Retrieved from https://doi.org/10.1038/s43247-020-0004-z doi: 10.1038/s43247-020-0004-z

Hunfeld, L. B., Chen, J., Hol, S., Niemeijer, A. R., & Spiers, C. J. (2020). Healing behavior of simulated fault gouges from the groningen gas field and implications for induced fault reactivation. *Journal of Geophysical Research: Solid Earth*, *125*(7), e2019JB018790. Retrieved from https://agupubs.onlinelibrary.wiley.com/doi/abs/10.1029/2019JB018790 (e2019JB018790 2019JB018790) doi: https://doi.org/10.1029/2019JB018790

Idehara, K., Yabe, S., & Ide, S. (2014, December). Regional and global variations in the temporal clustering of tectonic tremor activity. *Earth, Planets and Space*, *66*(1), 66. doi: 10.1186/1880-5981-66-66

Ingleby, T., & Wright, T. J. (2017). Omori-like decay of postseismic velocities following continental earthquakes. *Geophysical Research Letters*, *44*(7), 3119-3130. Retrieved from https://agupubs.onlinelibrary.wiley.com/doi/abs/10.1002/2017GL072865 doi: https://doi.org/10.1002/2017GL072865

Jaeger, J. C., & Cook, N. G. W. (1979). *Fundamentals of rock mechanics.* Cambridge UK: Chapman and Hall.

Kachanov, L. M. (1958). On rupture time under condition of creep. *Izvestia Akademi Nauk SSSR, Otd. Tekhn. Nauk*, *8*, 26–31. ((in Russian))

Kostoglodov, V., Singh, S. K., Santiago, J. A., Franco, S. I., Larson, K. M., Lowry, A. R., & Bilham, R. (2003). A large silent earthquake in the guerrero seismic gap, mexico. *Geophysical Research Letters*, *30*(15), 1807. doi: 10.1029/2003GL017219

Lacroix, P., Perfettini, H., Taipe, E., & Guillier, B. (2014). Coseismic and postseismic motion of a landslide: Observations, modeling, and analogy with tectonic faults. *Geophysical Research Letters*, *41*(19), 6676-6680. Retrieved from https://agupubs.onlinelibrary.wiley.com/doi/abs/10.1002/2014GL061170 doi: https://doi.org/10.1002/2014GL061170

Li, Y.-G., & Vidale, J. E. (2001). Healing of the shallow fault zone from 1994–1998 after the 1992 m7.5 landers, california, earthquake. *Geophysical Research Letters*, *28*(15), 2999-3002. Retrieved from https://agupubs.onlinelibrary.wiley.com/doi/abs/10.1029/2001GL012922 doi: https://doi.org/10.1029/2001GL012922

Li, Y.-G., Vidale, J. E., Aki, K., Xu, F., & Burdette, T. (1998). Evidence of shallow fault zone strengthening after the 1992 ¡i¿m¡/i¿7.5 landers, california, earthquake. *Science*, *279*(5348), 217-219. Retrieved from https://www.science.org/doi/abs/10.1126/science.279.5348.217 doi: 10.1126/science.279.5348.217

Liu, Y., & Rice, J. R. (2005). Aseismic slip transients emerge spontaneously in three-dimensional rate and state modeling of subduction earthquake sequences. *Journal of Geophysical Research: Solid Earth*, *110*(B8). Retrieved from https://agupubs.onlinelibrary.wiley.com/doi/abs/10.1029/2004JB003424 doi: https://doi.org/10.1029/2004JB003424

Liu, Y., & Rice, J. R. (2007). Spontaneous and triggered aseismic deformation transients in a subduction fault model. *Journal of Geophysical Research: Solid Earth*, *112*(B9). Retrieved from https://agupubs.onlinelibrary.wiley.com/doi/abs/10.1029/2007JB004930 doi: https://doi.org/10.1029/2007JB004930

Luo, Y., & Liu, Z. (2019). Rate-and-state model casts new insight into episodic tremor and slow-slip variability in cascadia. *Geophysical Research Letters*, *46*(12), 6352-6362. doi: https://doi.org/10.1029/2019GL082694

Luo, Y., & Liu, Z. (2021). Fault zone heterogeneities explain depth-dependent pattern and evolution of slow earthquakes in cascadia. *Nature Communications*, *12*(1), 1959. doi: 10.1038/s41467-021-22232-x

Lyakhovsky, V., Ben-Zion, Y., & Agnon, A. (1997). Distributed damage, faulting and friction. *Journal of Geophysical Research*, *102*(B12), 27635-27649.

Lyakhovsky, V., Ben-Zion, Y., & Agnon, A. (2001). Earthquake cycle, fault zones, and seismicity patterns in a rheologically layered lithosphere. *Journal of Geophysical Research: Solid Earth*, *106*(B3), 4103-4120. Retrieved from https://agupubs.onlinelibrary.wiley.com/doi/abs/10.1029/2000JB900218 doi: https://doi.org/10.1029/2000JB900218

Lyakhovsky, V., Reches, Z., Weinberger, R., & Scott, T. E. (1997). Non-linear elastic behaviour of damaged rocks. *Geophysical Journal International*, *130*(1), 157-166. Retrieved from https://onlinelibrary.wiley.com/doi/abs/10.1111/j.1365-246X.1997.tb00995.x doi: https://doi.org/10.1111/j.1365-246X.1997.tb00995.x

McLaskey, G. C., Thomas, A. M., Glaser, S. D., & Nadeau, R. M. (2012). Fault healing promotes high-frequency earthquakes in laboratory experiments and on natural faults. *Nature*, *491*(7422), 101–104. Retrieved from https://doi.org/10.1038/nature11512 doi: 10.1038/nature11512

Michael, A. J. (2011). Random variability explains apparent global clustering of large earthquakes. *Geophysical Research Letters*, *38*(21). Retrieved from https://agupubs.onlinelibrary.wiley.com/doi/abs/10.1029/2011GL049443 doi: https://doi.org/10.1029/2011GL049443

Nur, A., & Mavko, G. (1974). Postseismic viscoelastic rebound. *Science*, *183*(4121), 204-206. Retrieved from https://www.science.org/doi/abs/10.1126/science.183.4121.204 doi: 10.1126/science.183.4121.204

Obara, K. (2002). Nonvolcanic deep tremor associated with subduction in southwest japan. *Science*, *296*(5573), 1679–1681. Retrieved from https://science.sciencemag.org/content/296/5573/1679 doi: 10.1126/science.1070378

Obara, K., & Kato, A. (2016). Connecting slow earthquakes to huge earthquakes. *Science*, *353*(6296), 253–257. Retrieved from https://science.sciencemag.org/content/353/6296/253 doi: 10.1126/science.aaf1512

Ólason, E., Rampal, P., & Dansereau, V. (2021). On the statistical properties of sea-ice lead fraction and heat fluxes in the arctic. *The Cryosphere*, *15*(2), 1053–1064. Retrieved from https://tc.copernicus.org/articles/15/1053/2021/ doi: 10.5194/tc-15-1053-2021

Omori, F. (1894). On the aftershocks of earthquakes. *Journal of the College of Science, Imperial University of Tokyo*, *7*, 111–120.

Parisio, F., Vinciguerra, S., Kolditz, O., & Nagel, T. (2019). The brittle-ductile transition in active volcanoes. *Scientific Reports*, *9*(1), 143. Retrieved from https://doi.org/10.1038/s41598-018-36505-x doi: 10.1038/s41598-018-36505-x

Payero, J. S., Kostoglodov, V., Shapiro, N., Mikumo, T., Iglesias, A., Pérez-Campos, X., & Clayton, R. W. (2008). Nonvolcanic tremor observed in the mexican subduction zone. *Geophysical Research Letters*, *35*(7), L07305. doi: 10.1029/2007GL032877

Peacock, S. M. (2009). Thermal and metamorphic environment of subduction zone episodic tremor and slip. *Journal of Geophysical Research: Solid Earth*, *114*(B8). Retrieved from `https://agupubs.onlinelibrary.wiley.com/doi/abs/10.1029/2008JB005978` doi: https://doi.org/10.1029/2008JB005978

Peng, Z., & Gomberg, J. (2010). An integrated perspective of the continuum between earthquakes and slow-slip phenomena. *Nature Geoscience*, *3*, 599–607. doi: https://doi.org/10.1038/ngeo940

Perfettini, H., & Avouac, J.-P. (2004). Postseismic relaxation driven by brittle creep: A possible mechanism to reconcile geodetic measurements and the decay rate of aftershocks, application to the chi-chi earthquake, taiwan. *Journal of Geophysical Research: Solid Earth*, *109*(B2). doi: https://doi.org/10.1029/2003JB002488

Periollat, A., Radiguet, M., Weiss, J., Twardzik, C., Amitrano, D., Cotte, N., ... Socquet, A. (2022). Transient brittle creep mechanism explains early postseismic phase of the 2011 tohoku-oki megathrust earthquake: Observations by high-rate gps solutions. *Journal of Geophysical Research: Solid Earth*, *127*(8), e2022JB024005. doi: https://doi.org/10.1029/2022JB024005

Poiata, N., Vilotte, J.-P., Shapiro, N. M., Supino, M., & Obara, K. (2021). Complexity of deep low-frequency earthquake activity in shikoku (japan) imaged from the analysis of continuous seismic data. *Journal of Geophysical Research: Solid Earth*, *126*(11), e2021JB022138. doi: https://doi.org/10.1029/2021JB022138

Poli, P. (2017). Creep and slip: Seismic precursors to the nuugaatsiaq landslide (greenland). *Geophysical Research Letters*, *44*(17), 8832-8836. Retrieved from `https://agupubs.onlinelibrary.wiley.com/doi/abs/10.1002/2017GL075039` doi: https://doi.org/10.1002/2017GL075039

Pollitz, F. F. (2003). Transient rheology of the uppermost mantle beneath the mojave desert, california. *Earth and Planetary Science Letters*, *215*(1), 89 - 104. Retrieved from `http://www.sciencedirect.com/science/article/pii/S0012821X03004321` doi: https://doi.org/10.1016/S0012-821X(03)00432-1

Pollitz, F. F. (2005). Transient rheology of the upper mantle beneath central alaska inferred from the crustal velocity field following the 2002 denali earthquake. *Journal of Geophysical Research: Solid Earth*, *110*(B8). Retrieved from `https://agupubs.onlinelibrary.wiley.com/doi/abs/10.1029/2005JB003672` doi: https://doi.org/10.1029/2005JB003672

Pollitz, F. F., Wicks, C., & Thatcher, W. (2001). Mantle flow beneath a continental strike-slip fault: Postseismic deformation after the 1999 hector mine earthquake. *Science*, *293*(5536), 1814-1818. Retrieved from `https://www.science.org/doi/abs/10.1126/science.1061361` doi: 10.1126/science.1061361

Popov, A., & Sobolev, S. V. (2008). Slim3d: A tool for three-dimensional thermomechanical modeling of lithospheric deformation with elasto-visco-plastic rheology. *Physics of the Earth and Planetary Interiors*, *171*(1), 55-75. Retrieved from `https://www.sciencedirect.com/science/article/pii/S003192010800054X` (Recent Advances in Computational Geodynamics: Theory, Numerics and Applications) doi: https://doi.org/10.1016/j.pepi.2008.03.007

Radiguet, M., Cotton, F., Vergnolle, M., Campillo, M., Walpersdorf, A., Cotte, N., & Kostoglodov, V. (2012). Slow slip events and strain accumulation in the guerrero gap, mexico. *Journal of Geophysical Research: Solid Earth*, *117*(B4). Retrieved from `https://agupubs.onlinelibrary.wiley.com/doi/abs/10.1029/2011JB008801` doi: https://doi.org/10.1029/2011JB008801

Radiguet, M., Perfettini, H., Cotte, N., & et al. (2016). Triggering of the 2014 Mw 7.3 Papanoa earthquake by a slow slip event in guerrero, mexico. *Nature Geoscience*, *9*, 829–833. doi: https://doi.org/10.1038/ngeo2817

Rampal, P., Dansereau, V., Olason, E., Bouillon, S., Williams, T., Korosov, A.,

& Samaké, A. (2019). On the multi-fractal scaling properties of sea ice deformation. *The Cryosphere*, *13*(9), 2457–2474. Retrieved from https://tc.copernicus.org/articles/13/2457/2019/ doi: 10.5194/tc-13-2457-2019

Renard, F., Gratier, J.-P., & Jamtveit, B. (2000). Kinetics of crack-sealing, intergranular pressure solution, and compaction around active faults. *Journal of Structural Geology*, *22*(10), 1395-1407. Retrieved from https://www.sciencedirect.com/science/article/pii/S019181410000064X doi: https://doi.org/10.1016/S0191-8141(00)00064-X

Rivet, D., Campillo, M., Shapiro, N. M., Cruz-Atienza, V., Radiguet, M., Cotte, N., & Kostoglodov, V. (2011). Seismic evidence of nonlinear crustal deformation during a large slow slip event in mexico. *Geophysical Research Letters*, *38*(8). Retrieved from https://agupubs.onlinelibrary.wiley.com/doi/abs/10.1029/2011GL047151 doi: https://doi.org/10.1029/2011GL047151

Rogers, G., & Dragert, H. (2003). Episodic tremor and slip on the cascadia subduction zone: The chatter of silent slip. *Science*, *300*(5627), 1942–1943. Retrieved from http://www.jstor.org/stable/3834528

Royden, L. H., Burchfiel, B. C., King, R. W., Wang, E., Chen, Z., Shen, F., & Liu, Y. (1997). Surface Deformation and Lower Crustal Flow in Eastern Tibet. *Science*, *276*(5313), 788–790. doi: 10.1126/science.276.5313.788

Ruina, A. (1983). Slip instability and state variable friction laws. *Journal of Geophysical Research: Solid Earth*, *88*(B12), 10359-10370. Retrieved from https://agupubs.onlinelibrary.wiley.com/doi/abs/10.1029/JB088iB12p10359 doi: https://doi.org/10.1029/JB088iB12p10359

Saramito, P. (2020). *Efficient c++ finite element computing with rheolef.* CNRS-CCSD ed. (http://hal.archives-ouvertes.fr/cel-00573970)

Savage, J., Svarc, J., & Yu, S.-B. (2005). Postseismic relaxation and transient creep. *Journal of Geophysical Research: Solid Earth*, *110*(B11).

Scholz, C. H. (1998). Earthquakes and friction laws. *Nature*, *391*, 37-42.

Segall, P., & Bradley, A. M. (2012). The Role of Thermal Pressurization and Dilatancy in Controlling the Rate of Fault Slip. *Journal of Applied Mechanics*, *79*(3). Retrieved from https://doi.org/10.1115/1.4005896 (031013) doi: 10.1115/1.4005896

Segall, P., & Rice, J. R. (1995). Dilatancy, compaction, and slip instability of a fluid-infiltrated fault. *Journal of Geophysical Research: Solid Earth*, *100*(B11), 22155-22171. Retrieved from https://agupubs.onlinelibrary.wiley.com/doi/abs/10.1029/95JB02403 doi: https://doi.org/10.1029/95JB02403

Seydoux, L., Balestriero, R., Poli, P., de Hoop, M., Campillo, M., & Baraniuk, R. (2020). Clustering earthquake signals and background noises in continuous seismic data with unsupervised deep learning. *Nature Communications*, *11*(1), 3972. Retrieved from https://doi.org/10.1038/s41467-020-17841-x doi: 10.1038/s41467-020-17841-x

Shapiro, N. M., Campillo, M., Kaminski, E., Vilotte, J.-P., & Jaupart, C. (2018). Low-frequency earthquakes and pore pressure transients in subduction zones. *Geophysical Research Letters*, *45*(20), 11,083-11,094. doi: https://doi.org/10.1029/2018GL079893

Shcherbakov, R., Turcotte, D. L., & Rundle, J. B. (2005). Aftershock statistics. *Pure and applied geophysics*, *162*(6), 1051-1076.

Shelly, D. R., Beroza, G. C., Ide, S., & Nakamura, S. (2006). Low-frequency earthquakes in shikoku, japan, and their relationship to episodic tremor and slip. *Nature*, *442*(7099), 188–191. doi: 10.1038/nature04931

Sibson, R. H. (1992). Implications of fault-valve behaviour for rupture nucleation and recurrence. *Tectonophysics*, *211*(1), 283 - 293. Retrieved from http://www.sciencedirect.com/science/article/pii/004019519290065E doi: https://doi.org/10.1016/0040-1951(92)90065-E

Siravo, G., Faccenna, C., Gérault, M., Becker, T. W., Fellin, M. G., Herman, F., & Molin, P. (2019). Slab flattening and the rise of the eastern cordillera, colombia. *Earth and Planetary Science Letters*, *512*, 100 - 110. Retrieved from `http://www.sciencedirect.com/science/article/pii/S0012821X19300925` doi: https://doi.org/10.1016/j.epsl.2019.02.002

Sun, T., & Wang, K. (2015). Viscoelastic relaxation following subduction earthquakes and its effects on afterslip determination. *Journal of Geophysical Research: Solid Earth*, *120*(2), 1329-1344. Retrieved from `https://agupubs.onlinelibrary.wiley.com/doi/abs/10.1002/2014JB011707` doi: https://doi.org/10.1002/2014JB011707

Tang, C. (1997). Numerical simulation of progressive rock failure and associated seismicity. *International Journal of Rock Mechanics and Mining Sciences*, *34*(2), 249-261.

Turcotte, D. L. (1992). *Fractals and chaos in geology and geophysics.* New York, NY, USA: Cambridge University Press.

Turcotte, D. L., Newman, W. I., & Shcherbakov, R. (2003). Micro and macroscopic models of rock fracture. *Geophysical Journal International*, *152*, 718-728.

van den Ende, M., Chen, J., Ampuero, J.-P., & Niemeijer, A. (2018). A comparison between rate-and-state friction and microphysical models, based on numerical simulations of fault slip. *Tectonophysics*, *733*, 273 - 295. Retrieved from `http://www.sciencedirect.com/science/article/pii/S0040195117305024` (Physics of Earthquake Rupture Propagation) doi: https://doi.org/10.1016/j.tecto.2017.11.040

Wang, K., Hu, Y., & He, J. (2012). Deformation cycles of subduction earthquakes in a viscoelastic Earth. *Nature*, *484*, 327–332. doi: https://doi.org/10.1038/nature11032

Wang, Q.-Y., Campillo, M., Brenguier, F., Lecointre, A., Takeda, T., & Hashima, A. (2019). Evidence of changes of seismic properties in the entire crust beneath japan after the mw 9.0, 2011 tohoku-oki earthquake. *Journal of Geophysical Research: Solid Earth*, *124*(8), 8924-8941. Retrieved from `https://agupubs.onlinelibrary.wiley.com/doi/abs/10.1029/2019JB017803` doi: https://doi.org/10.1029/2019JB017803

Wech, A. G., & Creager, K. C. (2011). A continuum of stress, strength and slip in the cascadia subduction zone. *Nature Geoscience*, *4*(9), 624–628. doi: 10.1038/ngeo1215

Weiss, J., & Dansereau, V. (2017). Linking scales in sea ice mechanics. *Philosophical Transaction Royal Society A: Mathematical, Physical and Engineering Sciences*, *375*(2086), 20150352. Retrieved from `http://rsta.royalsocietypublishing.org/content/375/2086/20150352` doi: 10.1098/rsta.2015.0352

Williams, R. T., Davis, J. R., & Goodwin, L. B. (2019). Do large earthquakes occur at regular intervals through time? a perspective from the geologic record. *Geophysical Research Letters*, *46*(14), 8074-8081. Retrieved from `https://agupubs.onlinelibrary.wiley.com/doi/abs/10.1029/2019GL083291` doi: https://doi.org/10.1029/2019GL083291

Williams, R. T., Mozley, P. S., Sharp, W. D., & Goodwin, L. B. (2019). U-th dating of syntectonic calcite veins reveals the dynamic nature of fracture cementation and healing in faults. *Geophysical Research Letters*, *46*(22), 12900-12908. Retrieved from `https://agupubs.onlinelibrary.wiley.com/doi/abs/10.1029/2019GL085403` doi: https://doi.org/10.1029/2019GL085403

Williams, T., Korosov, A., Rampal, P., & Ólason, E. (2019). Presentation and evaluation of the Arctic sea ice forecasting system neXtSIM-F. *The Cryosphere Discussions*, *2019*, 1–31. Retrieved from `https://tc.copernicus.org/preprints/tc-2019-154/` doi: 10.5194/tc-2019-154